Materials Today Bio 37 (2026) 102964

Contents lists available at ScienceDirect

Materials Today Bio

journal homepage: www.journals.elsevier.com/materials-today-bio

A sequential defense-nourishment strategy enabled by thermosensitive core-shell microneedles for synergistic tendon repair

Meimei Fu [a,b,1], Jintao Li [a,*,1], Yiwen Jiang [c,d,1], Yan Shao [a], Dianxuan Wu [a], Shaozi Zhong [a], Zhuoyi Huang [b], Chao Chen [a], Jinshan Guo [b,c,**], Denghui Xie [a,***], Chun Zeng [a,****]

[a] Department of Sports Medicine, Center for Orthopedic Surgery, Orthopedic Hospital of Guangdong Province, The Third School of Clinical Medicine, Southern Medical University, The Third Affiliated Hospital of Southern Medical University, Guangzhou, 510630, PR China
[b] Department of Histology and Embryology, School of Basic Medical Sciences, Southern Medical University, 1023 Southern Shatai Rd., Guangzhou, 510515, PR China
[c] Suzhou Institute of Biomedical Engineering and Technology, Chinese Academy of Science, Suzhou, 215011, PR China
[d] School of Materials Science and Engineering, Changchun University of Science and Technology, Changchun, 130022, PR China

ARTICLE INFO

Keywords:
Thermosensitive cross-linking
Microneedles
Platelet-Rich Plasma (PRP)
Proanthocyanidin-copper
Tendon repair
Sequential defense-nutrition strategy

ABSTRACT

Achilles tendon rupture is a common sports injury, yet clinical tendon repair remains challenging. Current therapeutic approaches lack the ability to temporally regulate the injury microenvironment, hindering the synergy between anti-inflammatory defense and tissue regeneration. To address this, an innovative "sequential defense nutrition" synergistic strategy based on thermosensitive core-shell microneedles is proposed for efficient repair of complex tendon injuries. The study designed and fabricated core-shell microneedles using thermosensitive hydroxybutyl chitosan (HBC) as the matrix, with a core encapsulating growth factor-rich platelet-rich plasma (PRP) and a shell loaded with a proanthocyanidin-copper metal-phenolic network (PCCu) possessing both antioxidant and antibacterial functions. Leveraging the temperature-responsive gelation of HBC, this intelligent delivery system achieves stable anchoring and sustained release after implantation, overcoming the limitation of conventional delivery systems that are prone to displacement in deep tissue. At the injury site, the PCCu in the shell rapidly releases first, clearing reactive oxygen species (ROS) and inhibiting bacterial proliferation to swiftly establish an anti-inflammatory and anti-infective microenvironment. Subsequently, the PRP core provides programmed sustained release of growth factors, continuously supplying bioactive signals necessary for the proliferation and differentiation of tendon-derived stem cells. *In vitro* experiments confirmed that the system exhibits excellent antioxidant and broad-spectrum antibacterial activities and effectively promotes tenogenic differentiation. In a rat Achilles tendon injury model, the microneedle patch significantly reduced inflammation, promoted aligned and dense collagen fiber deposition, and consequently enhanced the biomechanical strength of the tendon, achieving in situ functional regeneration of the tendon defect. This work is the first to combine thermosensitive core-shell microneedles with a "defense-nutrition" sequential delivery strategy, which holds promising application prospects in sports medicine and tissue engineering.

1. Introduction

Tendons, which serve as crucial mechanical tissues connecting muscles to bones, are frequently damaged due to sports activities or repetitive strain [1,2]. Severe tendon injuries affect more than 102.5 million adults each year [3]. Given the specialized structure of tendon tissue and its high-stress physiological environment, extensive tendon injuries are often accompanied by complex repair challenges, including

This article is part of a special issue entitled: Multiscale Composites published in Materials Today Bio.

* Corresponding author.
** Corresponding author. Department of Histology and Embryology, School of Basic Medical Sciences, Southern Medical University, 1023 Southern Shatai Rd., Guangzhou, 510515, PR China.
*** Corresponding author.
**** Corresponding author.
E-mail addresses: lijintao4979@163.com (J. Li), jsguo4127@smu.edu.cn (J. Guo), xiedenghui221122@smu.edu.cn (D. Xie), zengdavid@126.com (C. Zeng).
[1] These authors contribute equally.

https://doi.org/10.1016/j.mtbio.2026.102964
Received 30 December 2025; Received in revised form 11 February 2026; Accepted 22 February 2026
Available online 26 February 2026

slow healing rates, high risk of re-rupture, and suboptimal functional recovery, all of which significantly impact patients' quality of life and rehabilitation [4,5]. The endogenous healing capacity of tendon tissue is inherently limited, primarily due to its unique biological characteristics, which include low metabolic activity, along with low cellular and vascular density [6,7]. These intrinsic properties impede the initiation of effective self-repair mechanisms following injury. Furthermore, post-injury inflammatory responses and the risk of infection further complicate treatment, thereby restricting high-quality tendon regeneration and functional restoration [8,9] (see Scheme 1).

Tendon repair strategies currently encompass surgical suturing, physical therapy, and local application of bioactive factors [10]. Although conventional conservative treatments and surgical interventions can alleviate symptoms to some extent, they often fall short of achieving genuine tissue regeneration and functional restoration [11]. Clinical observations indicate that tendon tissues after routine treatments frequently exhibit disorganized collagen fiber alignment and compromised mechanical properties, significantly impairing patients'

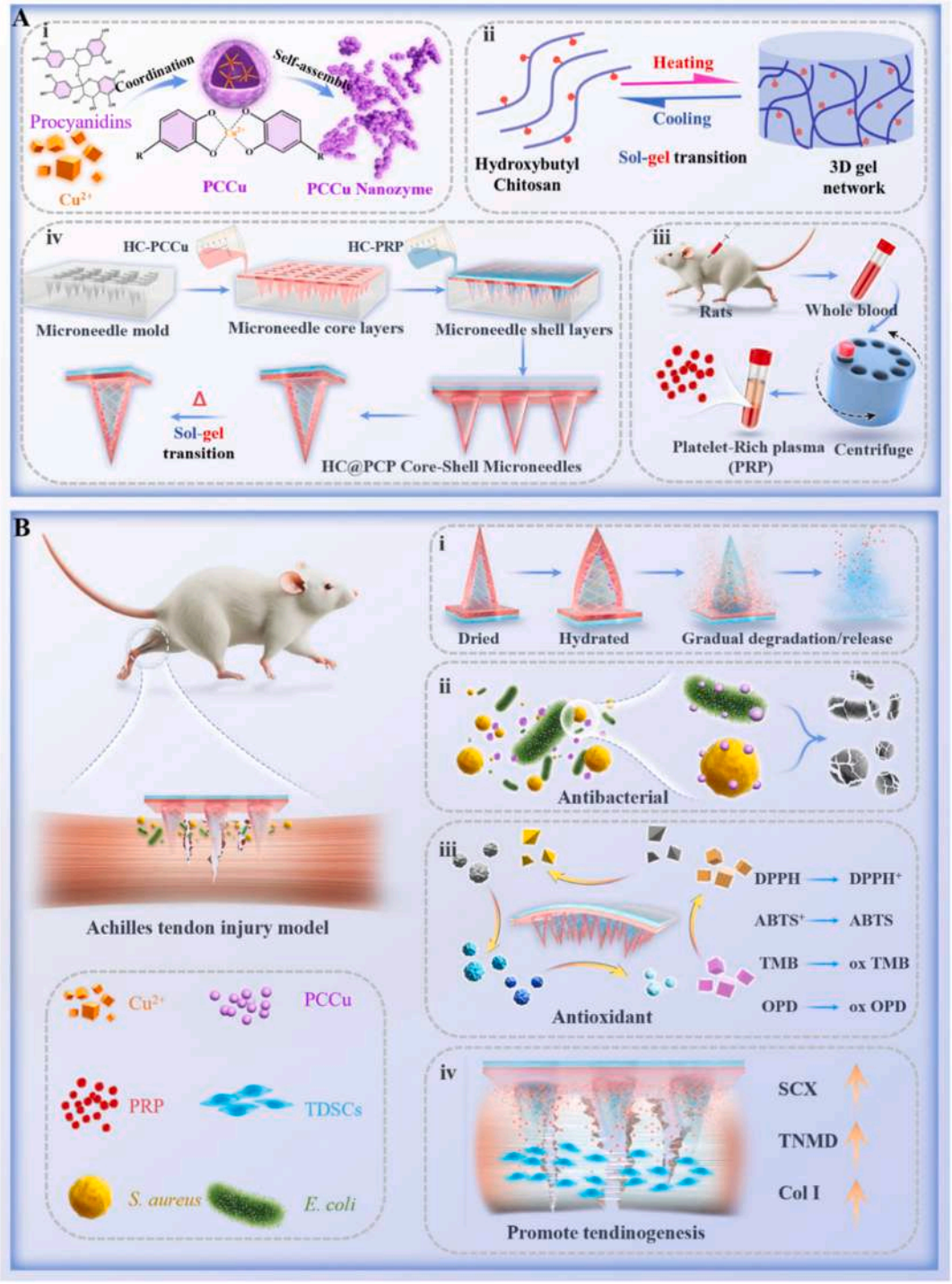

Scheme 1. A sequential defense-nourishment strategy enabled by thermosensitive core-shell microneedles for synergistic tendon repair. (A) Schematic flowchart of the fabrication process for HC@PCP microneedles. (B) Schematic diagram illustrating the regulatory mechanism of HC@PCP in promoting high-quality tendon healing in a rat Achilles tendon injury model.

quality of life and functional recovery [12]. In response to the inherent limitations of endogenous tendon healing, platelet-rich plasma (PRP) therapy has been introduced to promote tendon repair through the release of multiple growth factors [13,14]. However, the standalone application of PRP at injury sites presents limitations such as instability in bioactivity, transient therapeutic effects, and susceptibility to the local inflammatory microenvironment, which collectively constrain its full therapeutic potential [15]. Moreover, tendon injury sites are typically characterized by persistent inflammatory responses, excessive accumulation of reactive oxygen species (ROS), and secondary infection risks, all of which constitute an adverse microenvironment that impedes effective tissue regeneration [16]. Concurrently, post-injury oxidative stress and potential infections further diminish the activity of growth factors within PRP, thereby weakening its therapeutic efficacy [17]. An ideal tendon repair strategy must address two critical fronts: providing growth factors for "nutritional" support, and implementing "defensive" measures through early intervention. The latter aims to mitigate oxidative stress and inflammation, control infection, and thus clear the path for subsequent regeneration [18]. Therefore, developing an intelligent delivery system capable of temporally regulating the injury microenvironment and synergistically integrating both defensive and nutritional functions, simultaneously addressing inflammation, infection, and extracellular matrix reconstruction, holds significant scientific merit and application value for achieving efficient tendon repair.

In recent years, microneedle (MN) technology has emerged as a minimally invasive and efficient transdermal drug delivery platform, demonstrating considerable potential in tissue repair [19]. Traditional drug delivery systems often face limitations such as poor tissue penetration, uncontrollable drug release, and low bioavailability, which hinder their ability to meet the diverse demands of complex tissue injury repair [20,21]. Particularly in the field of tendon repair, achieving efficient drug delivery to deep tissues while maintaining the bioactivity and sustained release of therapeutic factors remains a key technological bottleneck that restricts treatment efficacy [22]. Notably, thermosensitive material-based microneedles leverage their temperature-responsive sol-gel transition properties to achieve in situ solidification and long-term retention after administration, ensuring localized sustained drug release and thus offering significant application potential for tendon-targeted drug delivery [23,24]. Hydroxybutyl chitosan (HBC), as an intelligent biomaterial with thermosensitive characteristics, exhibits a unique sol-gel transition that enables rapid gelation under physiological temperature, allowing the microneedles to achieve stable anchoring within tissues [25,26]. This temperature-responsive behavior not only ensures mechanical strength during insertion but also forms a stable drug reservoir after implantation, facilitating the sustained release of therapeutic agents [27,28]. Meanwhile, metal-phenolic networks (MPNs) have attracted widespread attention in the construction of functional biomaterials owing to their straightforward preparation, excellent antioxidant and antibacterial properties, and favorable biocompatibility [29,30]. Integrating MPNs with thermosensitive microneedle systems holds promise for equipping the latter with early-stage active defense capabilities against the injury microenvironment.

Therefore, this study proposes for the first time an innovative sequential defense-nutrition synergistic repair strategy, achieved by designing and fabricating a core-shell structured composite microneedle patch based on thermosensitive HBC. The patch features a shell loaded with a proanthocyanidin-copper metal-phenolic network (PCCu) possessing antioxidant and antibacterial functions, and a core encapsulating platelet-rich plasma (PRP) rich in multiple growth factors. This unique structural design enables the spatiotemporally separated loading of therapeutic agents. Moreover, leveraging the temperature-responsive gelation of HBC ensures firm anchoring and sustained release of the microneedles within the tissue, thus overcoming the limitations of traditional single-modality therapeutic strategies. Through systematic *in vitro* experiments, the physicochemical properties, antioxidant and antibacterial activities, and tenogenic differentiation-promoting capacity of the composite microneedle patch were evaluated. Furthermore, in a rat Achilles tendon defect model, its significant efficacy in reducing inflammation, promoting the formation of aligned collagen fibers, and accelerating functional tendon recovery through the sequential defense-nutrition mechanism was validated. This "defense first, nutrition second" sequential treatment paradigm effectively addresses the inadequacy of conventional single-modality strategies in managing complex pathological processes, offering a novel technological pathway for tendon regenerative medicine.

2. Materials and methods

2.1. Materials

Chitosan (CS), 1,2-buteneoxide, procyanidins (PC), and copper (II) sulfate hexahydrate ($CuSO_4{\cdot}6H_2O$) were purchased from Shanghai Macklin Biochemical Co., Ltd. All chemicals were used without further purification. Polydimethylsiloxane (PDMS) molds were purchased from Taizhou Microchip Pharmaceutical Technology Co., Ltd. (Taizhou, China).

2.2. Synthesis and characterization of hydroxybutyl chitosan

To synthesize hydroxybutyl chitosan, 10 g of chitosan was treated with 50 mL of 50% (w/w) sodium hydroxide solution and allowed to stand at room temperature for 24 h. The alkalized chitosan was then dispersed in 200 mL of a mixed solvent consisting of isopropanol and water (1:1, v/v) and reacted for an additional 24 h. The resulting mixture was transferred into a three-necked flask, followed by the addition of 200 mL of 1,2-epoxybutane. The reaction was carried out under constant stirring at 55 °C for 12 h. After completion, the pH of the system was adjusted to neutral (pH 7) by dropwise addition of 1 mol/L hydrochloric acid. The product was then dialyzed against deionized water using a dialysis membrane with a molecular weight cut-off of 3500 Da for 3 days. The dialyzed solution was filtered and subsequently freeze-dried to obtain the purified hydroxybutyl chitosan (HBC).

The chemical structure of HBC was characterized by ^{1}H NMR spectroscopy (Bruker Ascend 400 MHz) and Fourier transform infrared (FT-IR) spectroscopy (Thermo Scientific Nicolet iS10). Its solubility behavior under different pH conditions was investigated by recording the optical density (OD) of hydroxybutyl chitosan solutions at a wavelength of 600 nm. The thermosensitive cross-linking behavior of the HBC hydrogel was first verified by vial-inversion tests conducted at room temperature and 37 °C. Subsequently, the phase transition temperature of the HBC hydrogel was determined through temperature-sweep experiments. Amplitude sweep measurements were performed by varying shear strain at a constant frequency to obtain G′ and G″. Finally, the morphology of the HBC hydrogel was observed using a field-emission scanning electron microscope (SEM, ZEISS SIGMA).

2.3. Synthesis of proanthocyanidin-copper (PCCu) nanozymes

To synthesize the PCCu nanozymes, 0.2 g of copper(II) sulfate hexahydrate ($CuSO_4{\cdot}6H_2O$) was first dissolved in 20 mL of deionized water under vigorous stirring. Subsequently, 0.2 g of proanthocyanidin was dissolved in another 20 mL of deionized water, and the pH of this solution was adjusted to 9 using an appropriate alkaline solution. The two solutions were then mixed homogeneously. The resulting reaction mixture was centrifuged at 8000 rpm for 10 min to collect the crude product. The collected material was further purified by washing with deionized water at least three times, followed by freeze-drying to obtain the purified PCCu nanozymes.

The morphology of PCCu was first examined using SEM (ZEISS SIGMA), and elemental mapping was performed to investigate the distribution of elements. Furthermore, the chemical structure of PCCu was

analyzed by FT-IR (Thermo Scientific, Nicolet-iS10). The crystal structure and elemental composition of PCCu were then characterized by X-ray diffraction (XRD, Bruker D8) and X-ray photoelectron spectroscopy (XPS, Thermo Fisher Scientific, Escalab 250Xi), respectively.

2.4. Extraction of PRP

Platelet-rich plasma (PRP) was isolated from rat whole blood using differential centrifugation. To ensure good batch consistency and reliable quality control, a standardized protocol with fixed centrifugation speed, time, temperature, and operational procedures was strictly followed. All PRP batches were prepared by the same experimenter to minimize operational variation. Briefly, whole blood was collected via cardiac puncture from anesthetized Sprague-Dawley rats into anticoagulant-treated tubes. The blood was first centrifuged at a low speed (approximately 1500 rpm) for 15 min to allow for initial separation of blood components. After centrifugation, three distinct layers were observed: the upper layer consisted of platelet-poor plasma with a small number of leukocytes, while the lower layer contained mainly red blood cells. The middle layer, corresponding to platelet-rich plasma, was carefully aspirated using a sterile pipette and transferred to a new sterile centrifuge tube. Subsequently, the collected plasma was centrifuged at a higher speed (approximately 3000 rpm) for 20 min to pellet the platelets. Finally, the supernatant was discarded, and the concentrated platelet pellet was collected as the PRP sample.

2.5. Release of PCCu from the microneedle shell and growth factors from PRP loaded in the microneedle core

To enable real-time monitoring and quantitative assessment of the release kinetics of growth factors (platelet-derived growth factor (PDGF) and epidermal growth factor (EGF)) from PRP, a core-shell microneedle model was fabricated, in which the PRP core was fully encapsulated within a polymeric shell. After sterilization under ultraviolet (UV) light, the microneedles were placed in a 24-well plate containing PBS solution and incubated continuously for 21 days in a humidified incubator at 37 °C with 5% CO_2. At predetermined time points (days 1, 3, 5, 7, 10, 14, 17, and 21), the culture supernatant was collected. The concentrations of PDGF and EGF were quantified using enzyme-linked immunosorbent assay (ELISA), and the cumulative release profiles were subsequently plotted.

Additionally, PCCu was loaded into the shell layer of the core-shell microneedles. The release of PC and Cu was investigated at 37 °C by immersing the microneedles in 0.1 M PBS (pH 7.4). At predetermined time points (1, 3, 5, 7, and 10 days), the concentrations of released PC and Cu were measured using a UV-Vis spectrophotometer (Shimadzu, UV-2600) and inductively coupled plasma-mass spectrometry (ICP-MS, iCAP PRO, Thermo Fisher Scientific, MA, USA).

2.6. Preparation and characterization of core-shell microneedles

The HBC, HC@PC, and HC@PCP microneedles were fabricated using a polydimethylsiloxane (PDMS) negative-positive mold method. The PDMS positive mold consisted of a 13.5 × 13.5 cm base and 225 conical microneedles arranged in a 15 × 15 array. For HC@PCP microneedles, 10% (w/v) PCCu was uniformly dispersed in a 10% (w/v) HBC solution to prepare the needle-tip precursor. Then, 500 μL of this precursor solution was added into the PDMS negative mold and centrifuged to fully fill the microneedle cavities, followed by insertion of the PDMS positive mold for imprinting. After drying at room temperature for 24 h, the mold was demolded to obtain the microneedle tips containing PCCu. Subsequently, 1000 μL of an HBC solution loaded with an equivalent volume of PRP was added into the same mold to completely cover the base. After centrifugation to remove air bubbles, the system was dried for 72 h under constant conditions (25 °C, 50% humidity) before final demolding, yielding the complete core-shell structured HC@PCP microneedles. HC@PC and HBC microneedles were prepared following the same procedure. HC@PC microneedles were fabricated with PCCu incorporated only in the outer needle-tip layer, while the inner layer consisted of HBC solution only. HBC microneedles were prepared using pure HBC solution throughout the entire process.

The morphology of HC@PCP microneedles was observed using a stereomicroscope (Shuyu SZN71, China) and SEM. Elemental mapping was performed to characterize the distribution of key elements. To visually demonstrate the core-shell structure, microneedles were fabricated with rhodamine B (replacing PCCu) and calcein (replacing PRP) as fluorescent markers and examined under a fluorescence microscope (Olympus CKX41, Tokyo, Japan). To investigate their temperature-responsive behavior, the microneedles loaded with the colorimetric agent Rhodamine B were immersed in solutions maintained at 37 °C and monitored in real time. To evaluate the mechanical performance of the microneedles, penetration into rat skin was first examined, followed by compressive mechanical testing using an Instron 34TM-10 tensile tester. During compression testing, the lower plate was moved vertically downward at a constant speed of 0.5 mm/min until the microneedles bent or fractured, while the load-displacement curve of the microneedle array was recorded in real time.

2.7. In vitro antioxidant ability of core-shell microneedles

2.7.1. DPPH radical scavenging activity

The antioxidant activity of the core-shell microneedles was evaluated using the 2,2-Diphenyl-1-picrylhydrazyl (DPPH) free radical scavenging assay. A microneedle sample (5 mm × 5 mm) was immersed in 3.0 mL of an ethanolic DPPH solution (100 μM). After thorough mixing, the reaction system was incubated in the dark for a predetermined period. The absorbance was then measured at a wavelength of 517 nm using a UV-Vis spectrophotometer (Shimadzu 2600i, Japan). The DPPH scavenging activity was calculated according to the following formula:

$$\text{DPPH scavenging}\ (\%) = \frac{A_B\text{-}A_S}{A_B} \times 100\% \quad (1)$$

where A_B represents the absorbance of the blank control (DPPH solution without sample), and A_S represents the absorbance of the sample group (DPPH solution containing the microneedle sample).

2.7.2. $ABTS^+$ radical scavenging activity

The $ABTS^+$ radical working solution was prepared according to the manufacturer's protocol by mixing 2,2′-azino-bis(3-ethylbenzothiazoline-6-sulfonic acid) (ABTS) diammonium salt solution with potassium persulfate solution, followed by reaction in the dark for 12 h. The resulting solution was then diluted with phosphate-buffered saline (PBS, pH 7.4) to an appropriate concentration. Subsequently, a microneedle sample was added to the diluted $ABTS^+$ working solution and allowed to react in the dark for a predetermined duration. The absorbance of each reaction system was measured at 750 nm using a UV-Vis spectrophotometer, and recorded as the sample absorbance (A_S). A control without the sample was prepared in parallel, and its absorbance was measured as the blank absorbance (A_B). The $ABTS^+$ radical scavenging activity was calculated using Equation (2):

$$\text{ABTS scavenging}\ (\%) = \frac{A_B\text{-}A_S}{A_B} \times 100\% \quad (2)$$

2.7.3. Evaluation of POD-enzyme-like activity

The peroxidase-like activity of the core-shell microneedles was evaluated based on the catalytic oxidation of substrates TMB (3,3′,5,5′-tetramethylbenzidine) and OPD (o-phenylenediamine) to oxTMB (oxidized 3,3′,5,5′-tetramethylbenzidine) and oxOPD (2,3-Diaminophenazine), respectively, in the presence of H_2O_2 [31]. Briefly, the catalytic reaction was initiated by adding the microneedle sample to PBS (pH 4.0, 1.0 mL) containing H_2O_2 (20.0 μL, 0.5 M) and TMB (20.0 μL,

16.0 mM). The reaction progress was monitored by measuring the absorbance of oxTMB at 652 nm at specified time intervals using a UV-Vis spectrophotometer. Additionally, the oxidation product of OPD, oxOPD, was quantified by detecting its characteristic absorbance at 440 nm.

2.7.4. In vitro evaluation of the antioxidant capacity

This study assessed the cellular antioxidant capacity of HC@PCP microneedles using a reactive oxygen species (ROS) detection kit, with tendon-derived stem cells (TDSCs) selected for the experiment. Cells were seeded into a 24-well plate at a density of 10,000 cells per well, followed by a 30-min pretreatment with hydrogen peroxide (H_2O_2). Complete DMEM containing HC@PCP microneedle extract was then added, and the cells were incubated at 37 °C for 24 h. After incubation, the cells were washed with PBS. DCFH-DA was diluted at a 1:1000 ratio in serum-free medium, and 0.5 mL of the prepared DCFH-DA solution was added to each well. After 20 min of treatment, cellular fluorescence signals were analyzed using an inverted fluorescence microscope (Olympus CKX41, Tokyo, Japan), and fluorescence intensity was quantified using ImageJ software.

2.8. In vitro antimicrobial study

The antibacterial performance of the microneedles was evaluated against representative bacterial strains, including the Gram-positive bacterium *Staphylococcus aureus (S. aureus)* and the Gram-negative bacterium *Escherichia coli* (*E. coli*). The sterilized microneedles were placed in a 24-well plate, and 1 mL of bacterial suspension (approximately 1×10^6 colony-forming units (CFU)/mL) was added onto the surface of each sample. Untreated bacterial suspensions served as the control. All groups were incubated at 37 °C for 24 h. After incubation, the bacterial suspensions were diluted and subjected to a spread plate method for quantitative analysis. The plates were further incubated at 37 °C for another 24 h, after which the colonies were counted. To examine morphological changes of the bacteria, the co-cultured suspensions were dropped onto glass slides, fixed with 2.5% glutaraldehyde, dehydrated using a graded ethanol series, and finally observed by SEM.

To verify the early rapid defense function of HC@PCP microneedles, their bactericidal kinetic curves against common pathogenic bacteria in tendon injuries (*S. aureus* and *E. coli*) were determined. Briefly, 1 mL of bacterial suspension (10^5 CFU/mL) was directly co-cultured with materials from different treatment groups (including blank control and HC@PCP microneedle group) under shaking conditions (37 °C, 120 rpm). Samples were collected at 1, 2, 3, and 4 h, and the colony-forming units at different time points were quantitatively detected using the plate counting method. The relative bacterial growth inhibition rate was then calculated.

2.9. In vitro hemolysis assay

The hemocompatibility of the microneedles was evaluated using an *in vitro* hemolysis assay. Four experimental groups were designed: a negative control group (PBS), a positive control group (0.1% Triton X-100), an HBC microneedle group, and an HC@PCP microneedle group. Each material was co-incubated with fresh anticoagulated whole blood at 37 °C for 1 h. After incubation, the samples were centrifuged, and the supernatant was collected to measure its absorbance at 540 nm for subsequent calculation of the hemolysis rate.

2.10. In vitro cell experiments

2.10.1. Isolation and culture of TDSCs

Four-week-old male Sprague-Dawley rats were euthanized by cervical dislocation. The Achilles tendons were aseptically isolated and minced into approximately 1 mm × 1 mm fragments, followed by digestion with type I collagenase for 1 h to isolate tendon-derived stem cells (TDSCs). The digested mixture, including undigested tendon tissue, was then seeded in alpha-modified Eagle's medium (α-MEM) supplemented with 10% fetal bovine serum (FBS) and 1 × penicillin-streptomycin. After 48 h of culture, non-adherent cells were removed. When cells reached 100% confluence, they were passaged for expansion. Cells were expanded to passage 1 (P1) and subsequently cultured to passage 3 (P3), at which point they were used for subsequent experiments.

2.10.2. Biocompatibility of core-shell microneedles in vitro

To evaluate the cytotoxicity of the core-shell microneedles, the sterilized microneedles were first immersed in 10 mL of basal medium for 7 days to prepare the extraction solution. The cytotoxicity was then assessed using a Cell Counting Kit-8 (CCK-8, Servicebio, China). Tendon-derived stem cells (TDSCs) were co-cultured with the microneedle extract for 24 and 48 h, respectively, and cell viability was measured at each time point. Additionally, cells were stained using a Live/Dead Viability/Cytotoxicity Assay Kit (L32250, Thermo Fisher Scientific), and their morphology was observed under an inverted fluorescence microscope.

2.10.3. Cell immunofluorescence of tendon-specific markers

To investigate the effect of core-shell microneedles on the tenogenic differentiation of tendon-derived stem cells (TDSCs), the cells were cultured for 3 days in complete α-MEM medium containing different microneedle extracts. After culture, the cells were washed twice with PBS and fixed with 4% paraformaldehyde (PFA). Subsequently, the samples were blocked with 1% bovine serum albumin (BSA, Servicebio, China) and incubated overnight at 4 °C with primary antibodies, including anti-SCX (1:200), anti-TNMD (1:200), and anti-Col I (1:200) (Abmart, China). The following day, the samples were washed three times with PBS and incubated with a secondary antibody (Abcam, USA) at 37 °C for 2 h. After removal of the secondary antibody, cell nuclei were stained with DAPI (Beyotime, China) for 5 min. Finally, immunofluorescence images were observed and captured using an inverted fluorescence microscope. In addition, the expression levels of SCX, TNMD, and Col I in tendon-derived stem cells were quantitatively measured according to the instructions of the enzyme-linked immunosorbent assay (ELISA) kit.

2.11. In vivo animal studies

Male Sprague-Dawley (SD) rats (weighing 250-300 g) were purchased from the Laboratory Animal Center of Southern Medical University. All animal experiments were approved by the Animal Ethics Committee of the Institute of Biomedical Engineering, Guangdong Academy of Sciences (Approval No. 2024-01-157) and were conducted in strict accordance with the Guidelines for the Care and Use of Laboratory Animals. A total of 60 SD rats were randomly assigned to two observation time points (4 weeks and 8 weeks). At each time point, the rats were divided into four treatment groups: (1) Control group: Achilles tendon injury model was established followed by suture only, (2) HBC microneedle group: HBC microneedles were implanted after modeling and suture, (3) HC@PC microneedle group: HC@PC microneedles were implanted after modeling and suture, (4) HC@PCP microneedle group: HC@PCP microneedles were implanted after modeling and suture. The Achilles tendon injury model was established based on previously published methods. Under adequate analgesia, anesthesia, and surgical site disinfection, a longitudinal skin incision (approximately 2 cm in length) was made on the lateral aspect of the hind limb to expose the Achilles tendon. A 2 mm transverse incision was then made at the calcaneal tuberosity to simulate tendon rupture [32]. The severed tendon was sutured using a modified Kessler technique with 6-0 silk suture. Subsequently, the corresponding microneedles were implanted according to the assigned groups for treatment.

At 4 and 8 weeks post-operation, SD rats were euthanized, and the

regenerated tendon, along with surrounding tissues, was harvested. The samples were fixed in 4% paraformaldehyde and stored at 4 °C. After dehydration and paraffin embedding, tissue sections of 4 μm thickness were prepared and subjected to hematoxylin and eosin (H&E), Masson's trichrome, and Sirius red staining. H&E and Masson-stained sections were observed under an upright microscope (Olympus IX71SBF-2). Inflammatory cells in defined regions of H&E-stained sections were counted, and collagen content in Masson-stained sections was analyzed using ImageJ software. Sirius red-stained sections were examined under polarized light microscopy, and collagen fiber alignment was quantified with ImageJ. For tissues collected at the 8-week time point, immunohistochemical staining was performed for SCX and TNMD, and the sections were observed using an upright fluorescence microscope. Semi-quantitative analysis of SCX- and TNMD-positive cells was conducted with ImageJ. Biomechanical analysis was performed on harvested muscle-tendon-bone complexes (n = 5) at week 8. The calcaneus (bone) and the tendon-muscle junction were securely fixed in custom clamps. Following a 0.1 N preload, uniaxial tensile testing was conducted at a constant displacement rate of 5 mm/min until failure. The maximum force recorded during the test was defined as the failure load. The Young's modulus was calculated as the slope of the linear elastic region of the stress-strain curve. Failure strain was calculated as the ratio of the maximum displacement at rupture to the original gauge length of the tendon sample, representing the maximum deformation capacity before structural failure. To evaluate *in vivo* safety, H&E staining was performed on major organs (heart, liver, spleen, lung, and kidney) on week 8 for histological examination.

2.12. Statistical analysis

All quantitative data were statistically analyzed using GraphPad Prism 9 (GraphPad Software Inc., USA). Statistical significance between

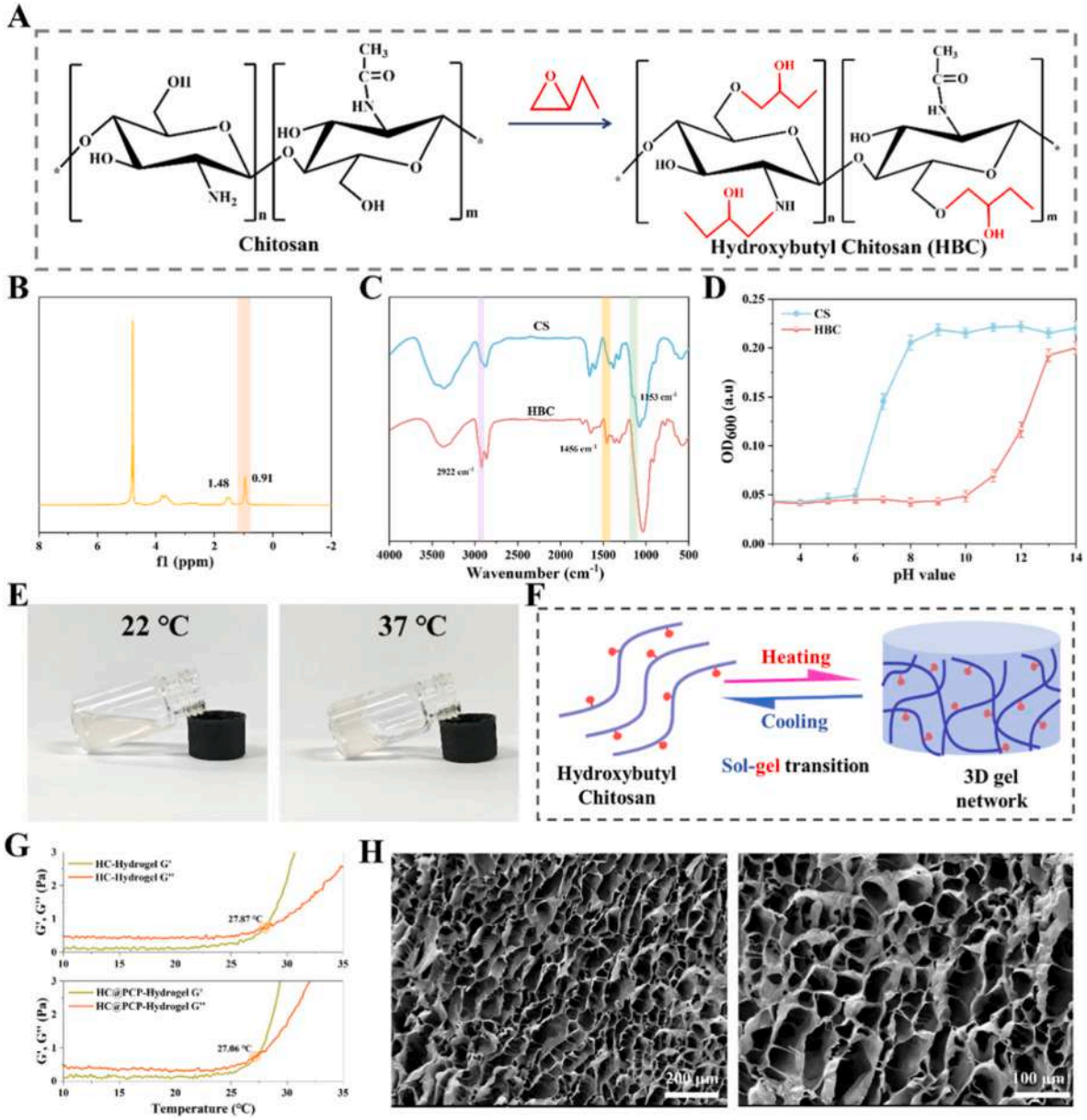

Fig. 1. Synthesis and characterization of hydroxybutyl chitosan. (A) Synthetic reaction scheme of hydroxybutyl chitosan (HBC). (B) ^{1}H NMR spectrum of HBC. (C) FTIR spectra of chitosan (CS) and HBC. (D) pH-dependent solubility profiles of chitosan and hydroxybutyl chitosan. (E) Macroscopic morphology of the thermosensitive HBC hydrogel. (F) Schematic diagram of the thermosensitive HBC hydrogel structure. (G) Temperature-sweep experimental results of HBC and HC@PCP hydrogels. (H) SEM image of HC@PCP hydrogel.

groups was determined by Student's t-test or one-way analysis of variance (ANOVA). A p-value less than 0.05 was considered statistically significant and is indicated by the symbol *. Different levels of significance are denoted as follows: * for $p < 0.05$, ** for $p < 0.01$, and *** for $p < 0.001$.

3. Results and discussion

3.1. Synthesis and characterization of hydroxybutyl chitosan

As shown in Fig. 1A, hydroxybutyl chitosan (HBC) was synthesized via the etherification of chitosan with 1,2-epoxybutane, resulting in the grafting of hydroxybutyl side chains onto the hydroxyl (-OH) and/or amino groups of the chitosan backbone [33]. Chitosan contains reactive hydroxyl and amino groups, allowing for both hydroxyl and amino substitution reactions with hydroxybutyl groups. In this study, the synthesis of HBC was conducted under alkaline conditions, favoring hydroxyl substitution to form ether linkages. In the ^{1}H NMR spectrum of HBC (Fig. 1B), a new signal at 0.91 ppm can be assigned to the methyl protons of the hydroxybutyl side chain [34]. FTIR spectral analysis revealed that, compared with chitosan, HBC exhibits new characteristic absorption peaks at 2922 cm^{-1} and 1456 cm^{-1}, corresponding to the C-H stretching and bending vibrations of methyl groups, respectively, confirming the successful grafting of hydroxybutyl groups onto the chitosan backbone (Fig. 1C) [35]. Moreover, the characteristic peak of chitosan at 1053 cm^{-1} (attributed to the 6-OH group) was absent in the HBC spectrum, suggesting that hydroxybutyl substitution predominantly occurred at the 6-position hydroxyl group [36]. Additionally, the absorption peak at 1377 cm^{-1} in the HBC infrared spectrum, attributed to C-N bending vibrations, also exhibits significant changes, indicating that partial hydroxybutyl substitution reactions have occurred at the C-NH_2 sites of chitosan. Dissolution behavior analysis (Fig. 1D) revealed that chitosan was soluble only in dilute acid solutions and formed flocculent precipitates when the pH reached 8, with optical density stabilizing thereafter. In contrast, the synthesized HBC remained soluble over a broader pH range, showing changes in optical density only when pH exceeded 11. These results further confirm that the hydroxybutyl substitution disrupted the crystalline structure of chitosan and weakened its intramolecular and intermolecular hydrogen bonding.

As shown in Fig. 1E, vial-inversion tests visually demonstrated the thermosensitive behavior of the HBC solution: it remained flowable at room temperature (≈22 °C) and rapidly formed a stable non-flowing gel upon heating to 37 °C, exhibiting a typical sol-gel transition. The thermosensitivity of HBC hydrogel originates from the introduction of hydrophobic hydroxybutyl groups onto its molecular chain. Its thermosensitive sol-gel transition is attributed to the synergistic effects of hydrophobic interactions, hydrogen bond rearrangement, and temperature-dependent micellar assembly [33,37]. At low temperatures, HBC chains remain hydrated and dispersed in aqueous solution, with intermolecular forces dominating. The system is stabilized by extensive hydrogen bonding with water molecules and behaves as a highly fluid sol. When the temperature is increased to physiological temperature (approximately 37 °C), the thermal motion of water molecules intensifies and disrupts the hydration between hydroxybutyl groups and water. This shift allows hydrophobic interactions between the hydrophobic side chains to become the dominant driving force. Through aggregation and association of hydrophobic domains, HBC molecular chains rapidly form a physically crosslinked network, leading to a sharp increase in solution viscosity and thus transitioning into a stable hydrogel. In addition, the abundant hydroxyl and amino groups on the HBC backbone also contribute to intermolecular hydrogen bonding, which further stabilizes the gel network formed at elevated temperatures. These combined driving forces trigger spontaneous gelation, enabling in situ solidification without chemical crosslinkers or external irradiation. When the temperature decreases, hydration resumes, hydrophobic interactions weaken, and the crosslinked network dissociates, allowing the gel to reversibly revert to a sol state (Fig. 1F). Temperature-sweep experiments further quantitatively determined the phase-transition temperature (T_{gel}) of the HBC hydrogel to be 27.87 °C (Fig. 1G). Additionally, the amplitude sweep revealed a pronounced strain-stiffening behavior followed by strain-thinning/yielding (Fig. S1). Both G′ and G″ showed a non-monotonic dependence on shear strain, increasing to a maximum before decreasing, indicative of a rearrangeable and yield-stress network [38]. Notably, the incorporation of PCCu and PRP did not significantly alter the thermosensitive gelling properties of HBC. This result is attributed to the mild physical loading strategy used in this system: both PCCu (as metal-phenolic network particles) and PRP are distributed within the HBC gel network via physical loading, without introducing chemical crosslinking or obvious interference with the hydrophobic interactions and hydrogen bonds between HBC molecular chains. Therefore, the key characteristic of HBC to undergo in situ gelation near body temperature is well preserved, ensuring that the microneedle system can stably complete the sol-gel transition and achieve firm tissue anchoring after implantation. Moreover, the gelation temperature of HBC, which is above room temperature yet below physiological temperature (37 °C), indicates that rapid gelation can occur under near-physiological conditions, providing a crucial basis for its potential biomedical applications. SEM images revealed that the HC@PCP hydrogel exhibited a characteristic porous network structure (Fig. 1H). This structure possessed continuous pore walls and favorable three-dimensional interconnectivity, which not only facilitates the efficient diffusion of nutrients and metabolites but also provides a suitable physical scaffold for cell migration and tissue ingrowth. Therefore, by taking advantage of thermosensitive property of HBC, the HBC matrix remains in a pre-gel state at room temperature, which facilitates microneedle fabrication and shaping. After the microneedles are implanted *in vivo*, the HBC rapidly undergoes the hydrophobic aggregation-driven phase transition triggered by body temperature (~37 °C), forming a stable physically crosslinked gel network in situ at the defect site. This process requires no chemical crosslinkers or external energy input, enabling mild and self-sustained anchoring of the microneedle system. It further provides an ideal and highly biocompatible carrier platform for the programmed release of bioactive components in subsequent steps.

3.2. Synthesis and characterizations of PCCu nanozymes

As illustrated in Fig. 2A, PCCu was synthesized via the room-temperature coordination of proanthocyanidins (PC) with copper ions (Cu^{2+}) under alkaline conditions. The elevated reaction pH facilitated the deprotonation of catechol groups in PC, while sufficient Cu^{2+} concentration ensured the stable formation of the PCCu coordination complex. The morphology, structural characteristics, and chemical composition of PCCu were characterized using scanning electron microscopy (SEM) combined with energy-dispersive X-ray spectroscopy (EDS) mapping (Fig. 2B–D). SEM images revealed that PCCu formed nanoparticles with an average diameter of approximately 100 nm (Fig. 2B). EDS mapping further confirmed the uniform distribution of Cu within the PC matrix, indicating homogeneous coordination between Cu^{2+} and PC (Fig. 2C). Fourier-transform infrared (FTIR) spectroscopy was employed to analyze the functional group changes in PC and PCCu (Fig. 2E). In the FTIR spectrum of PC, the characteristic peak at 1610 cm^{-1} was assigned to the C=O stretching vibration, while the absorption around 1285 cm^{-1} originated from the vibration of aromatic hydroxyl groups [39]. Notably, the intensities of these peaks were significantly reduced or even disappeared in the PCCu spectrum. Concurrently, a new absorption peak appeared at 1490 cm^{-1} in the PCCu spectrum, attributed to the symmetric stretching vibration of carboxylate anions (COO^-) formed after coordination [30]. X-ray diffraction (XRD) was further utilized to investigate the crystal structures of PC and PCCu (Fig. 2F). The XRD pattern of PCCu exhibited characteristic diffraction peaks within the 20-30° (2θ) range. Compared

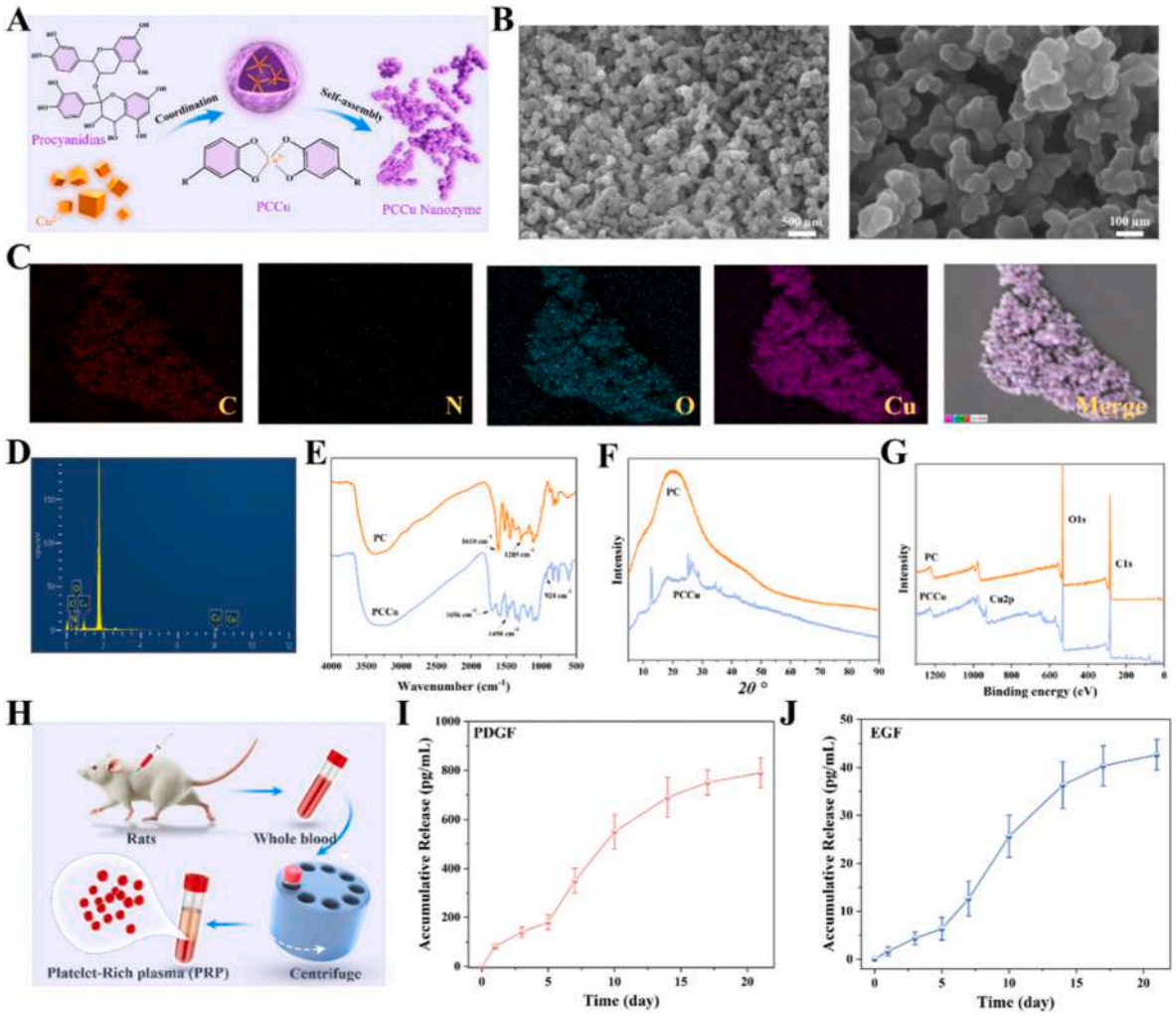

Fig. 2. Preparation and characterization of PCCu and PRP. (A) Schematic illustration of PCCu synthesis. (B) Scanning electron microscopy (SEM) image of PCCu. (C) Elemental mapping of PCCu. (D) EDS spectrum of PCCu. (E) Fourier transform infrared (FTIR) spectra of PC and PCCu. (F) X-ray diffraction (XRD) patterns of PC and PCCu. (G) X-ray photoelectron spectroscopy (XPS) spectra of PC and PCCu. (H) Schematic diagram of PRP extraction. Cumulative release profile of (I) PDGF and (J) EGF from PRP-loaded HBC hydrogel (n = 5).

with PC, the diffraction peaks of PCCu showed reduced intensity and shifts in peak positions, indicating that the formation of PCCu involved structural rearrangement and alterations in crystallinity. The crystalline structure of PCCu was clearly confirmed by high-resolution transmission electron microscopy (HRTEM) and selected area electron diffraction (SAED) (Fig. S2). HRTEM images (Fig. S2A and 2B) show that PCCu samples exhibit an aggregated morphology at the 100 nm scale, while distinct particle boundaries and clear lattice fringes can be observed at the 5 nm scale. The corresponding SAED pattern (Fig. S2C) displays characteristic diffraction spots and rings, indicating that PCCu is a polycrystalline powder. These results are in good agreement with the XRD data, jointly verifying the crystalline nature of PCCu. Additionally, XPS was used to analyze the chemical state of copper in PCCu (Fig. 2G). The binding energy peak at 935 eV was identified as Cu 2p, and the presence of satellite peaks further confirmed the existence of Cu^{2+} species. In comparison with the XPS spectrum of PC, the distinct appearance of copper signals in the PCCu spectrum directly verified the successful incorporation of Cu^{2+}.

3.3. Release of PRP and PCCu in core-shell HBC hydrogels

As shown in Fig. 2H, platelet-rich plasma (PRP) was successfully isolated from rat whole blood via differential centrifugation. Subsequently, the release behavior of growth factors from PRP-loaded core-shell HBC hydrogel microneedle was systematically evaluated. The cumulative release profiles (Fig. 2I and J) revealed that the growth factors (represented by PDGF and EGF) exhibited sustained and controllable release over a 21-day period. Specifically, the release occurred at a relatively slow rate during the initial phase (days 1-7), effectively avoiding the burst release of bioactive factors. From day 7 to day 21, the release rate of growth factors significantly accelerated, enabling long-term and stable supply of bioactive factors. This release profile is mainly determined by the dual barrier effect of the HBC hydrogel network and the core-shell structure. Growth factors encapsulated in the core are protected by the dense HBC hydrogel network and the outer shell layer, which slows down their diffusion rate at an early stage. Over time, the HBC hydrogel network gradually relaxes and undergoes slight degradation, reducing the diffusion resistance of growth factors and thereby achieving sustained and stable release. As for the release behavior of PC and Cu (the two components of PCCu), Fig. S3 shows that a distinct burst release pattern was observed. Specifically, within the initial 24 h of incubation, the cumulative release percentages of PC and Cu reached 50.5% and 48.65%, respectively, and the overall release process was nearly completed within 10 days. This rapid release behavior is attributed to the core-shell structural design and the thermosensitive gelation process of HBC. PCCu is loaded in the outer shell of

the hydrogel, where it directly contacts the release medium. During the initial sol-gel transition of HBC, the loose preliminary network formed creates abundant diffusion channels, allowing PCCu to diffuse rapidly out of the hydrogel matrix without being restricted by the dense core structure. The fast release of PCCu ensures that an effective concentration can be rapidly achieved at the injury site in the early stage, laying a solid foundation for scavenging reactive oxygen species (ROS) and inhibiting bacterial proliferation.

In summary, the release behaviors of PRP and PCCu are mainly attributed to the physical encapsulation and diffusion barrier effect of the HBC hydrogel network, together with the staged regulation of release kinetics by the core-shell structure [40]. The release kinetics of PCCu and growth factors show a clear temporal sequence: PCCu is released rapidly in the early and middle stages (0-10 days) to exert

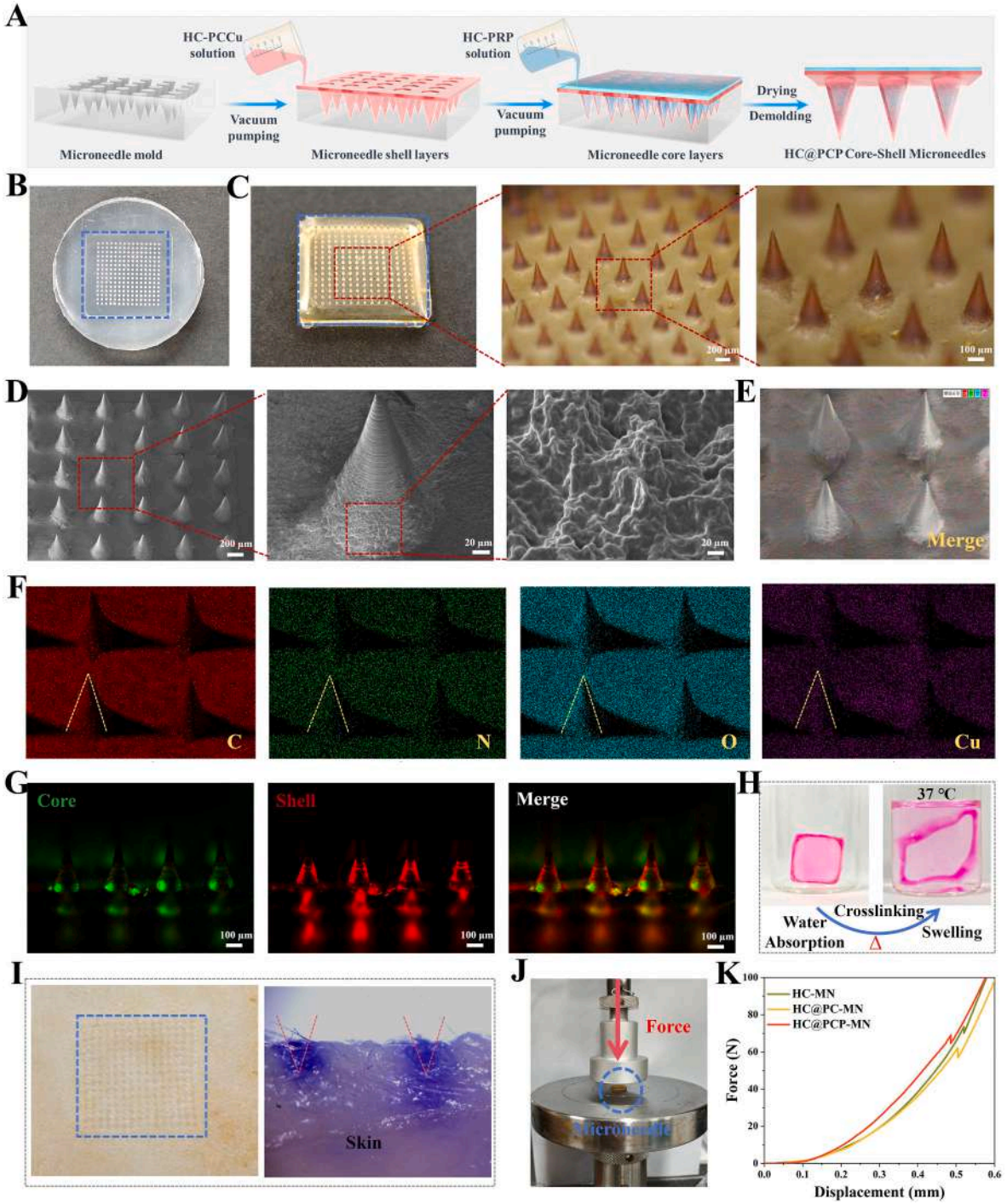

Fig. 3. Preparation and physical characterization of HC@PCP core-shell microneedles. (A) Schematic diagram of the fabrication process for core-shell microneedles. (B) Illustration of the polydimethylsiloxane (PDMS) mold. (C) Stereomicroscopy image of the core-shell microneedles. (D) Scanning electron microscopy (SEM) image of the core-shell microneedles. (E) Overlay elemental mapping of the microneedle surface. (F) Elemental distribution maps of C, N, O, and Cu elements on the microneedle surface. (G) Fluorescence microscopy image of the core-shell microneedles. (H) Observation of the thermosensitive cross-linking and swelling behavior of HBC microneedles. (I) Microscopic observation of microneedle skin penetration into rat skin. (J) Schematic illustration of the compression test on the microneedle array. (K) Compression load-displacement curves of the microneedle array.

anti-inflammatory and antibacterial effects, whereas growth factors are released continuously in the middle and late stages (5-21 days), providing long-term bioactive signals for tendon regeneration. Such coordinated sequential release clearly demonstrates the feasibility of the sequential "defense-nutrition" strategy designed in this study, and provides direct experimental support for the subsequent *in vitro* and *in vivo* functional evaluation of this system.

3.4. Characterization of core-shell microneedles

The fabrication process of the core-shell microneedles is illustrated in Fig. 3A. Specifically, the microneedles were prepared using a polydimethylsiloxane (PDMS) positive-negative mold method (Fig. 3B and S4). After demolding, the obtained HC@PCP microneedle array exhibited a regular 15 × 15 arrangement. Stereomicroscopic observation revealed a uniform conical morphology of the microneedles (Fig. 3C). Their surface morphology and microstructure were further characterized by scanning electron microscopy (SEM). As shown in Fig. 3D, the microneedle tips display a well-defined and intact pyramidal geometry with sharp apexes and no observable structural defects. The microneedle base exhibited a rough surface morphology, which could increase the contact area at the tissue interface, enhance frictional resistance after insertion, thereby improving mechanical anchoring and facilitating sustained drug release and therapeutic efficacy. Furthermore, elemental mapping images of HC@PCP (Fig. 3E and F) confirmed the homogeneous distribution of Cu^{2+} on the microneedle surface.

To verify the core-shell structure, microneedles were prepared using rhodamine B (simulating PCCu) and calcein (simulating PRP) as fluorescent markers. Fluorescence microscopy images showed a red outer layer and a green inner layer, indicating the successful construction of the core-shell architecture (Fig. 3G). The thermosensitive cross-linking behavior was further simulated *in vitro*. The HBC microneedles loaded

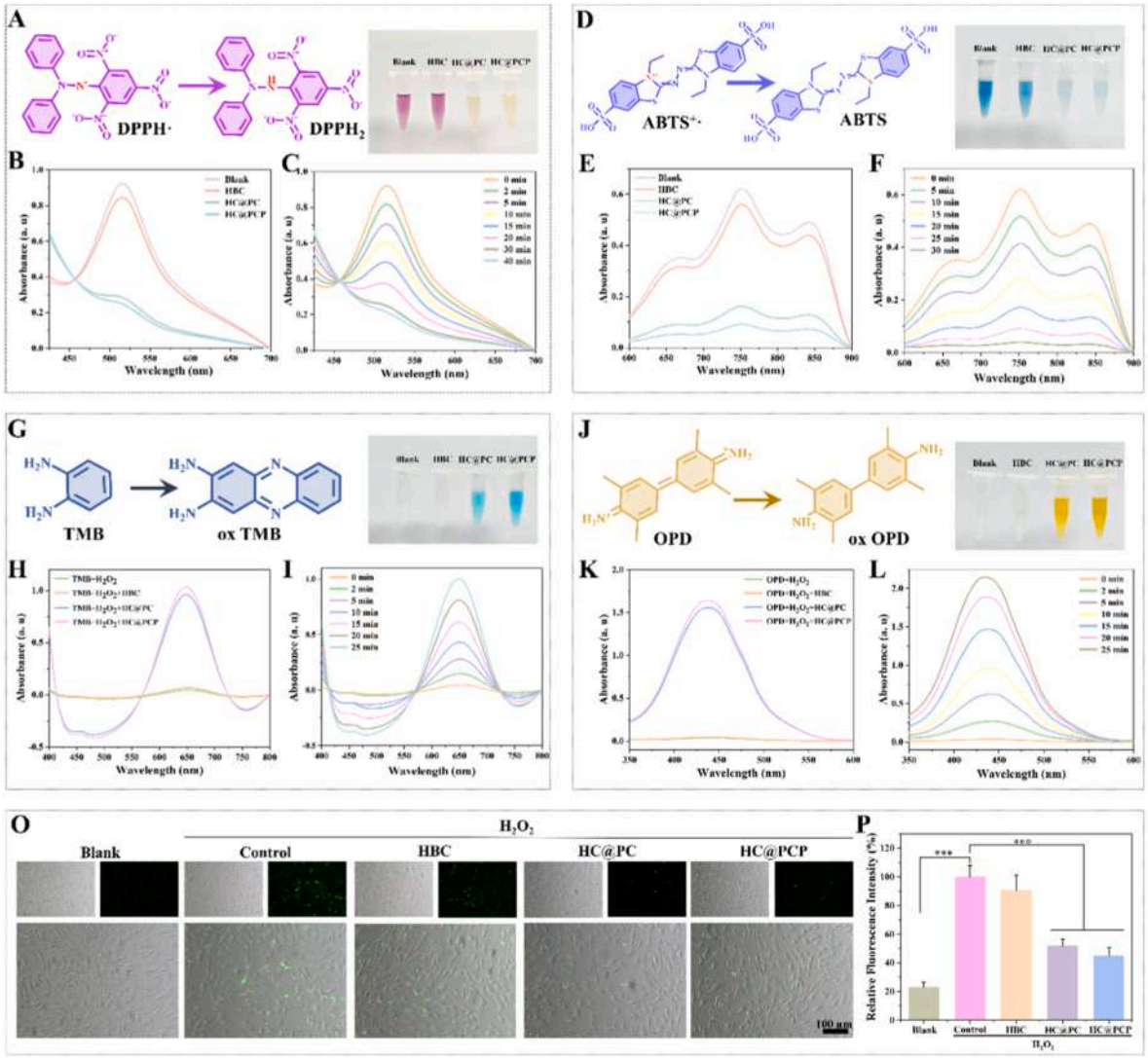

Fig. 4. *In vitro* antioxidant activity performance. (A) Photographs of different microneedles in DPPH solution after reaction and schematic of DPPH radical scavenging. (B) UV-Vis absorption spectra of DPPH solution treated with different microneedles. (C) Dynamic DPPH radical scavenging profile of HC@PCP. (D) Photographs of different microneedles in $ABTS^+$ solution after reaction and schematic of $ABTS^+$ radical scavenging. (E) UV-Vis absorption spectra of $ABTS^+$ solution treated with different microneedles. (F) Dynamic $ABTS^+$ radical scavenging profile of HC@PCP. (G) Photographs of different microneedles in TMB + H_2O_2 solution after reaction and schematic of TMB chromogenic reaction (oxidized to oxidized TMB(oxTMB)). (H) UV-Vis absorption spectra of the TMB reaction system with different microneedles. (I) Time-dependent UV-Vis spectral changes of the TMB reaction catalyzed by HC@PCP. (J) Photographs of different microneedles in OPD + H_2O_2 solution after reaction and schematic of OPD chromogenic reaction (oxidized to oxidized OPD(oxOPD)). (K) UV-Vis absorption spectra of the OPD reaction system with different microneedles. (L) Time-dependent UV-Vis spectral changes of the OPD reaction catalyzed by HC@PCP. (O) The fluorescence images and (P) relative fluorescence intensities of oxidation inhibition obtained by ROS test kit. $^*p < 0.05$, $^{**}p < 0.01$, $^{***}p < 0.001$.

with the colorimetric agent Rhodamine B exhibited significant swelling instead of dissolution in solution at 37 °C (Fig. 3H), confirming their potential for *in vivo* temperature-triggered gelation. In addition, after inserting HC@PCP into rat skin for 30 s and subsequent removal, orderly arranged micropores were observed on the skin surface, and crystal violet staining clearly demonstrated successful penetration of the microneedles through the skin tissue (Fig. 3I). Mechanical compression testing was performed on the microneedle arrays (Fig. 3J). The maximum failure force of the pure HBC microneedle array was about 70 N (Fig. 3K). In contrast, no significant change in the maximum failure force was observed for HC@PC and HC@PCP microneedle arrays, indicating that the incorporated components did not compromise the overall mechanical strength of the microneedles. These results demonstrate that the fabricated microneedles possess sufficient mechanical properties to effectively penetrate biological tissues such as skin and tendon [41].

3.5. In vitro antioxidant activity performance

Tendon injury typically triggers a local inflammatory response, leading to elevated levels of reactive oxygen species (ROS) that impede tendon regeneration [42]. Given the excellent antioxidant capacity of proanthocyanidins [16], we systematically characterized the antioxidant performance of PCCu. DPPH is a stable nitrogen-centered radical that appears purple in ethanol solution and exhibits a characteristic absorption peak at 517 nm [43], which can be used to quantitatively evaluate reducing capacity (Fig. 4A). As shown in Fig. 4B and S5, pure HBC microneedles displayed limited radical scavenging activity, scavenging only about 10.17% of DPPH radicals within 30 min. In contrast, the incorporation of PCCu significantly enhanced DPPH scavenging: HC@PC and HC@PCP achieved clearance rates of 78.36% and 83.02%, respectively, within 30 min. With prolonged time, the DPPH solution in the HC@PCP group became completely decolorized, and the absorption peak at 517 nm nearly disappeared, indicating nearly complete elimination of DPPH radicals (Fig. 4C and S6).

ABTS can be oxidized to form a stable bluish-green cationic radical ($ABTS^+$) with a characteristic absorption at 750 nm (Fig. 4D) [44]. Consistent with the DPPH results, HBC microneedles showed only weak $ABTS^+$ scavenging ability (Fig. 4E and S7). In contrast, PCCu-loaded HC@PC and HC@PCP exhibited pronounced $ABTS^+$ scavenging, with efficiencies reaching 73.36% and 80.16% within 25 min, respectively. Furthermore, the $ABTS^+$ scavenging rate of the HC@PCP group continued to increase over time (Fig. 4F and S8). These results demonstrate that HC@PCP possesses excellent antioxidant capacity, which is primarily derived from proanthocyanidins, while PRP also contributes partially to radical scavenging.

Moreover, the peroxidase-like activity of the microneedles was evaluated spectrophotometrically using 3,3′,5,5′-tetramethylbenzidine (TMB) and H_2O_2 as substrates (Fig. 4G–I). H_2O_2 can be catalytically converted by the microneedles to generate hydroxyl radicals (·OH), which subsequently oxidize TMB to oxTMB, producing a characteristic absorption peak at 652 nm (Fig. 4G). No significant absorption at 652 nm was observed in the TMB + H_2O_2 group or the TMB + H_2O_2 + HBC group, whereas both HC@PC and HC@PCP groups showed distinct peaks at this wavelength, confirming their peroxidase-like activity (Fig. 4H). Time-dependent catalytic experiments revealed that the absorption intensity of HC@PCP at 652 nm increased with time, demonstrating its time-responsive catalytic behavior (Fig. 4I). The peroxidase-like activity was further verified using the o-phenylenediamine (OPD) and H_2O_2 system (Fig. 4J–L). In the presence of peroxidase-like catalysts, OPD can be oxidized and polymerized by H_2O_2 to form 2,3-Diaminophenazine (oxOPD), which exhibits a characteristic absorption at 440 nm (Fig. 4J). The results were consistent with the TMB assay system: HC@PCP showed the highest peak intensity (Fig. 4K), and the absorbance peak of HC@PCP at 440 nm increased over time (Fig. 4L), confirming its time-dependent peroxidase-like catalytic activity.

The cellular antioxidant capacity of HC@PCP microneedles was evaluated using a reactive oxygen species (ROS) assay kit. In the experiment, H_2O_2 was used to stimulate cells to generate excessive intracellular ROS, while 2′,7′-dichlorodihydrofluorescein diacetate (DCFH-DA) served as the fluorescent probe to detect intracellular ROS levels. As shown in Fig. 4O and P, cells without H_2O_2 treatment exhibited almost no fluorescence signal, whereas the H_2O_2-treated group displayed strong fluorescence. Notably, cells treated with HC@PC and HC@PCP showed significantly lower DCFH fluorescence intensity compared to the H_2O_2-treated group, indicating effective intracellular ROS scavenging. In contrast, the HBC group without PCCu showed only a minor difference in fluorescence signal compared to the H_2O_2 group, suggesting that PCCu plays a key role in ROS clearance.

In summary, HC@PC and HC@PCP exhibited significant antioxidant and catalytic performance in DPPH/$ABTS^+$ scavenging assays, peroxidase-like activity tests and ROS scavenging assays, with PCCu serving as the primary active component. This system can effectively scavenge excess hydrogen peroxide and mitigate oxidative stress damage, providing a functional material basis for promoting tendon regeneration.

3.6. Antibacterial ability of the HC@PCP

The antibacterial effect was evaluated by co-incubating microneedles with bacterial suspensions. As shown in Fig. 5A, *Staphylococcus aureus* treated with HC@PC and HC@PCP exhibited a significant reduction in bacterial number and obvious damage to colony morphology. Bacterial viability was significantly lower than that of the control and HBC groups (Fig. 5B, $p < 0.001$). No significant difference was observed between the HC@PC and HC@PCP groups, while HBC also showed a certain inhibitory effect on *S. aureus*. These results indicate that HC@PCP possesses notable bacteriostatic and bactericidal activities against Gram-positive bacteria. Similarly, for *E. coli*, both HC@PC and HC@PCP treatment led to a marked decrease in bacterial count, accompanied by deformed and ruptured bacterial structures, and significantly reduced bacterial viability compared with the control and HBC groups, confirming the potent antibacterial activity of HC@PCP against Gram-negative bacteria (Fig. 5C and D). Overall comparison revealed that HBC itself exhibited a certain degree of antibacterial ability, whereas HC@PC and HC@PCP demonstrated the most pronounced antibacterial effects, suggesting a synergistic enhancement between PCCu and HBC (Fig. 5E). Moreover, the relatively weak antibacterial activity of pure HBC microneedles further indicated that PCCu serves as the primary active component responsible for the antimicrobial function [45].

The early growth inhibition kinetics of HC@PCP microneedles against *S. aureus* and *E. coli* were evaluated using a co-culture method. Both bacterial strains showed rapid proliferation within 4 h in the blank control group. In contrast, the HC@PCP microneedle group exhibited significant inhibition of bacterial proliferation as early as 1 h of co-culture, and the inhibitory effect was maintained continuously over 4 h. The relative growth inhibition rates reached 75.32% and 71.35% against *S. aureus* and *E. coli*, respectively (Fig. S9). In conclusion, HC@PCP displayed highly effective and broad-spectrum antibacterial performance against *S. aureus* and *E. coli*, which mainly stems from the synergistic antimicrobial activity of copper ions and proanthocyanidins in PCCu [30,46]. Furthermore, HC@PCP microneedles can rapidly suppress pathogen proliferation at the early injury stage, meeting the temporal requirement for early anti-infective defense. These results provide experimental evidence for the potential application of the sequential “defense-nutrition” strategy in the prevention and treatment of bacterial infection after tendon injury.

3.7. Hemocompatibility of HC@PCP

Good hemocompatibility is a prerequisite for the clinical application of biomedical materials [47]. To evaluate the biosafety of HC@PCP, an

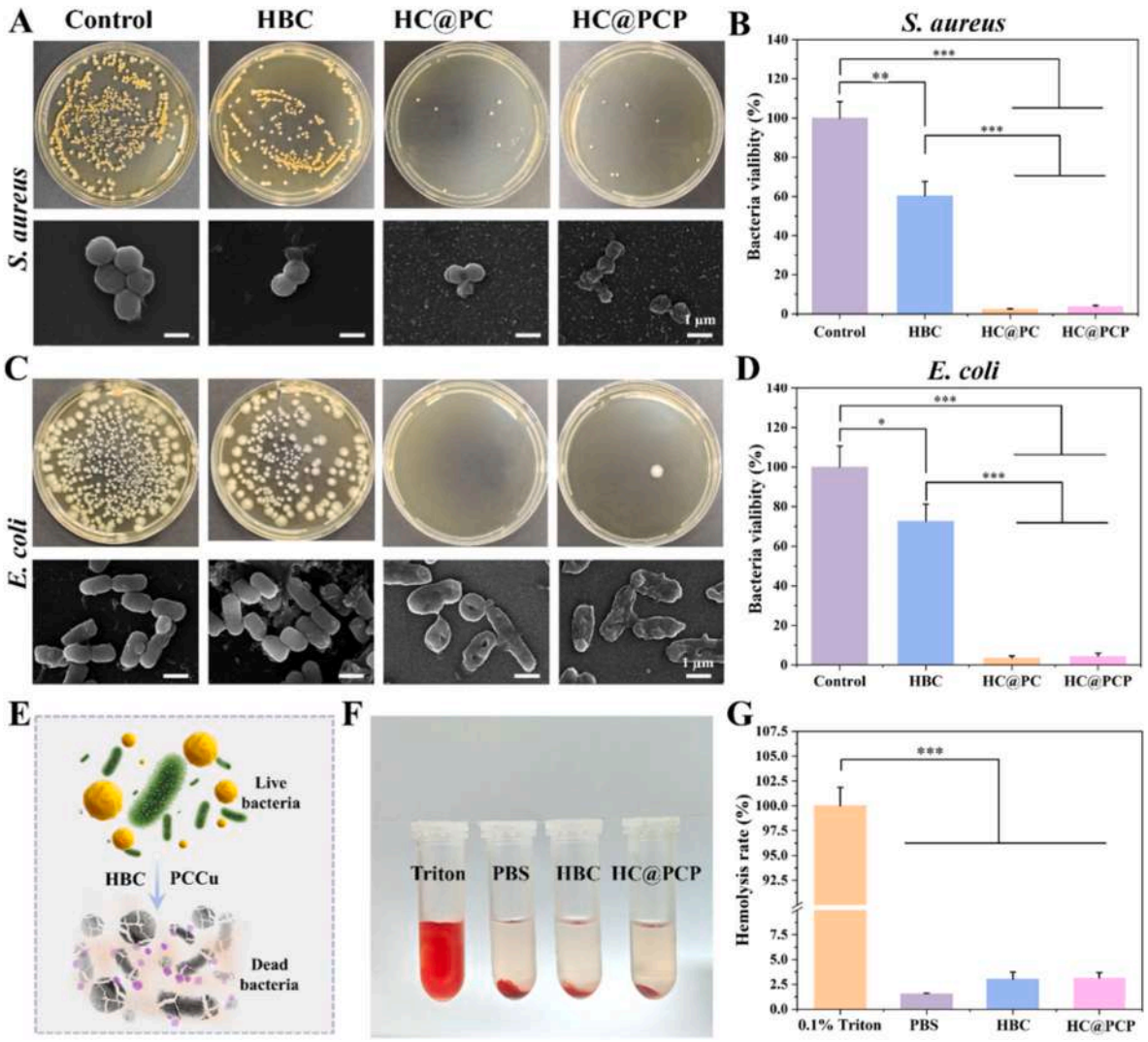

Fig. 5. Antibacterial ability and hemocompatibility of the HC@PCP. (A) Colony counting results and scanning electron microscopy (SEM) images of *S. aureus*. (B) Survival rates of *S. aureus* after treatment with different microneedles (n = 5). (C) Colony counting results and SEM images of *E. coli*. (D) Survival rates of *E. coli* after treatment with different microneedles (n = 5). (E) Schematic illustration of the antibacterial mechanism of HC@PCP microneedles. (F) Photographs of samples from the hemocompatibility test. (G) Relative hemolysis rates of different treatment groups (n = 5). $^{*}p < 0.05$, $^{**}p < 0.01$, $^{***}p < 0.001$.

in vitro hemocompatibility test was performed. As shown in Fig. 5F and G, the positive control group (0.1% Triton X-100) exhibited strong hemolytic effects with a hemolysis rate of 100%. In contrast, the PBS negative control group displayed only a very low background hemolysis rate, confirming the reliability of the experimental system. Both the HBC microneedle group and the HC@PCP group showed hemolysis rates comparable to the PBS group and significantly lower than that of the positive control group (Fig. 5G, $p < 0.001$). Notably, the hemolysis rate of HC@PCP was below 5%, meeting the commonly accepted safety threshold for hemocompatibility of biomaterials (<5%). In summary, these results demonstrate that HC@PCP possesses good hemocompatibility and fulfills the safety requirements for biomaterials.

3.8. Effects of HC@PCP on the viability and tenogenic differentiation of TDSCs

To evaluate the biocompatibility of HC@PCP and its effects on the viability and differentiation of tendon-derived stem cells (TDSCs), TDSCs were first treated with HC@PCP extract, and cell morphology and viability were observed using live/dead cell staining. As shown in Fig. 6A, at both 24 h and 48 h, cells in the control and all treatment groups (HBC, HC@PC, HC@PCP) maintained good adherence and spreading morphology, with no obvious shrinkage, floating, or death. CCK-8 quantitative results (Fig. 6B) indicated that after 24 h of culture, cell viability in all treatment groups showed no significant difference compared with the control. At 48 h, the viability of HC@PC and HC@PCP groups was significantly higher than that of the control ($p < 0.05$), with the HC@PCP group showing the most pronounced enhancement, suggesting that the combined loading of PCCu and PRP promotes TDSC proliferation activity.

The tenogenic differentiation of TDSCs was further assessed by immunofluorescence staining of key markers. SCX is an early key transcription factor in tendon development [48]. Compared with the control, HC@PC treatment significantly increased SCX fluorescence intensity (Fig. 6C and D, $p < 0.001$), indicating activation of upstream tenogenic pathways. The HC@PCP group exhibited even higher SCX expression than the HC@PC group ($p < 0.05$), demonstrating a synergistic enhancement effect with PRP incorporation. TNMD is a tendon-specific structural protein involved in collagen maturation and mechanical function [9]. Both HC@PC and HC@PCP treatments markedly enhanced TNMD fluorescence intensity (Fig. 6E and F, $p < 0.01$), indicating that the material system not only initiates differentiation but also promotes the synthesis of functional proteins. Meanwhile, expression of type I collagen (Col I), the main component of the tendon

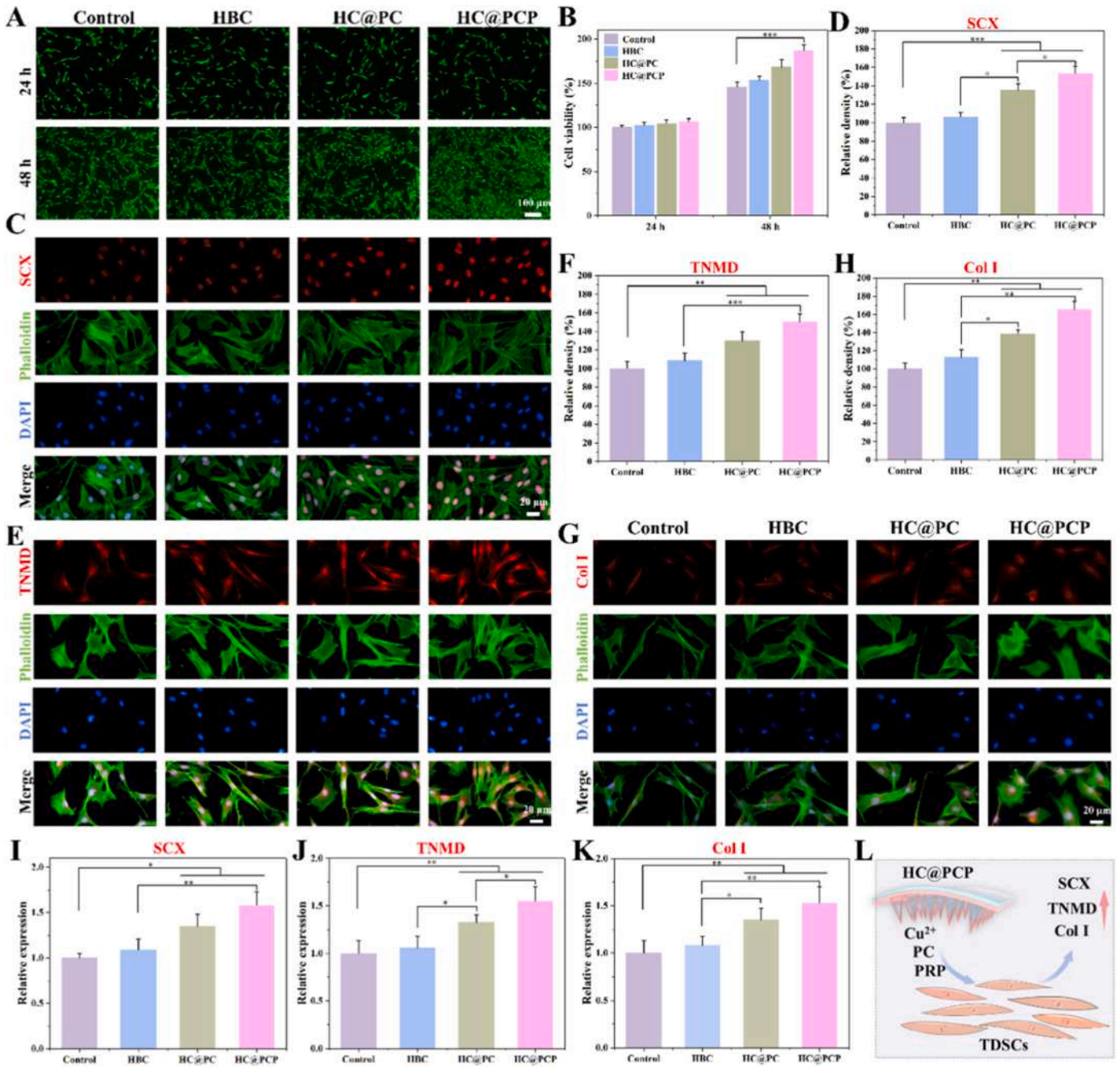

Fig. 6. Effects of HC@PCP on the cellular viability and tenogenic differentiation potential of TDSCs. (A) Representative fluorescence images of live/dead staining. (B) Statistical analysis of cell viability based on CCK-8 assay (n = 5). (C) Immunofluorescence staining images of SCX in TDSCs treated with different microneedles. (D) Quantitative analysis of SCX immunofluorescence intensity (n = 5). (E) Immunofluorescence staining images of TNMD in TDSCs treated with different microneedles. (F) Quantitative analysis of TNMD immunofluorescence intensity (n = 5). (G) Immunofluorescence staining images of Col I in TDSCs treated with different microneedles. (H) Quantitative analysis of Col I immunofluorescence intensity (n = 5). The mRNA relative expression levels of SCX (I), TNMD (J), and Col I (K) detected by qPCR (n = 5). (L) Schematic illustration of the synergistic mechanism of PRP and PCCu in promoting tenogenic differentiation of TDSCs. $^{*}p < 0.05$, $^{**}p < 0.01$, $^{***}p < 0.001$.

extracellular matrix, was also significantly increased in the HC@PCP group (Fig. 6G and H), which contributes to the formation of well-aligned collagen fibers and facilitates the restoration of tendon mechanical function. At the transcriptional level, qPCR results further confirmed these findings (Fig. 6I–K). Compared with the control (set as 1), the relative expression of SCX in the HC@PCP group increased to 1.58 ($p < 0.001$), TNMD increased from 1 to 1.54 ($p < 0.001$), and Col I expression was also significantly upregulated. These results consistently demonstrate that HC@PCP effectively promotes the expression of SCX, TNMD, and Col I in TDSCs, inducing their tenogenic differentiation. The observed tenogenic effects are primarily attributed to the synergistic action of PRP and PCCu (Fig. 6L). PRP is rich in various growth factors, such as PDGF, TGF-β, and IGF-1, which can upregulate tenogenic gene expression by activating signaling pathways such as TGF-β/Smad and PI3K/Akt [49]. Meanwhile, copper ions in PCCu serve as cofactors for enzymatic reactions involved in collagen cross-linking and energy metabolism, while proanthocyanidins alleviate oxidative stress through antioxidant activity, together providing a supportive microenvironment for the tenogenic differentiation of TDSCs [46,50].

3.9. Assessment of in vivo tendon repair efficac

To evaluate the therapeutic efficacy of the developed HC@PCP core-shell microneedles, a rat Achilles tendon rupture model was established and treated by local microneedle delivery. Tendon samples were collected at predetermined time points, and the repair outcomes among different groups were systematically compared (Fig. 7A). Histological analysis revealed that at 4 weeks post-operation, H&E staining showed fibroblast rearrangement and inflammatory cell infiltration in all groups (Fig. 7B). However, inflammatory cell counting demonstrated that both HC@PC and HC@PCP groups significantly reduced inflammatory cell density compared with the control and HBC groups (Fig. 7C). Moreover, the HC@PCP group exhibited the densest collagen structure and the most aligned collagen fiber orientation. At 8 weeks post-operation, tendon repair quality improved in all groups compared with that at 4 weeks (Fig. 7D), but disorganized and loose collagen fibers were still observed in the control and HBC groups, indicating insufficient local regeneration. In contrast, the HC@PC group displayed a large amount of newly formed, highly aligned collagen fibers. Notably, the HC@PCP group showed a more mature, dense, and highly ordered collagen architecture, which was further confirmed by quantitative statistical analysis (Fig. 7E). Sirius red staining indicated that collagen deposition became progressively denser over time in all groups (Fig. 7F). At 4 weeks, collagen fibers were not fully mature, and no significant differences in collagen content or fiber alignment were observed among the control, HBC, and HC@PC groups, whereas the HC@PCP group

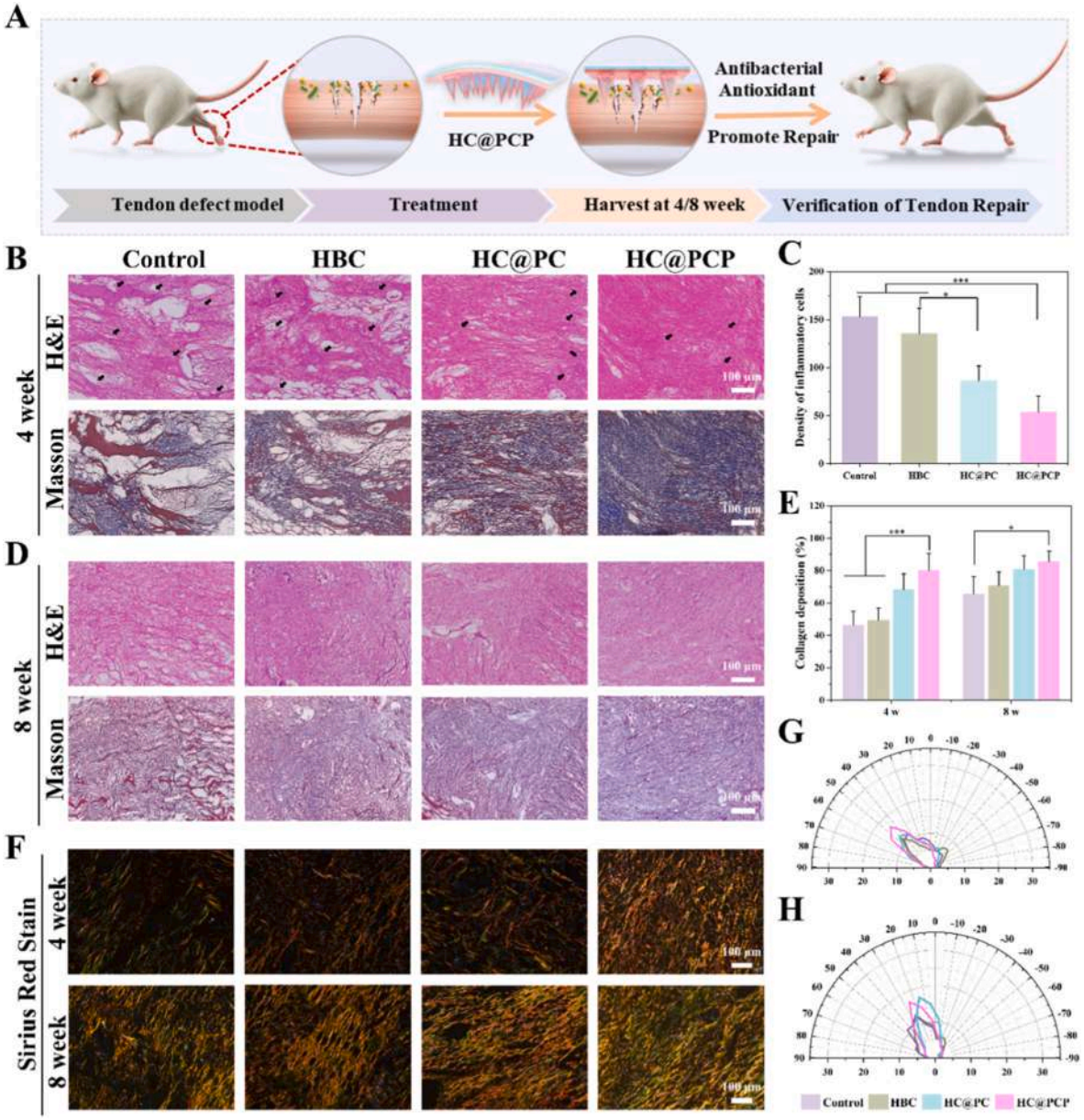

Fig. 7. Assessment of *in vivo* tendon repair efficacy. (A) Schematic diagram of the experimental procedure for microneedle treatment of Achilles tendon injury. (B) Representative H&E and Masson's trichrome staining images of Achilles tendon tissues at 4 weeks post-operation (black arrow: inflammatory cells). (C) Statistical analysis of inflammatory cell numbers in each group at 4 weeks post-operation (n = 5). (D) Representative H&E and Masson's trichrome staining images of Achilles tendon tissues at 8 weeks post-operation. (E) Quantitative analysis of collagen deposition in Achilles tendon tissues at 8 weeks post-operation (n = 5). (F) Representative Sirius red staining images of Achilles tendon tissues at 4 and 8 weeks post-operation. (G) Statistical analysis of collagen fiber orientation in each group at (G) 4 weeks post-operation and (H) 8 weeks post-operation.*$p < 0.05$, **$p < 0.01$, ***$p < 0.001$. (For interpretation of the references to color in this figure legend, the reader is referred to the Web version of this article.)

exhibited higher collagen deposition and more uniform fiber orientation (Fig. 7G). By 8 weeks, the HC@PCP group showed abundant, well-aligned type I collagen deposition, forming a mature extracellular matrix structure, while collagen deposition remained sparse and less organized in the control and HBC groups (Fig. 7H). The results above demonstrate that HC@PCP core-shell microneedles significantly promote collagen deposition, mature alignment, and regenerative quality in injured tendon tissue by establishing a microenvironment conducive to tendon regeneration, exhibiting promising therapeutic potential.

3.10. HC@PCP regulates the expression of key tendon regeneration markers SCX and TNMD in vivo

To investigate the regulatory role of HC@PCP on key tendon regeneration markers *in vivo*, this study employed immunofluorescence staining to evaluate the expression of SCX, an early marker of tendon differentiation, and TNMD, a terminal marker, in repaired tissues at 8 weeks post-surgery. Following tendon injury, early and effective tendon-specific differentiation is central to functional recovery. SCX, as a tendon-specific transcription factor, regulates the differentiation process of tendon stem cells into tendon cells. Compared with the control and HBC groups, the HC@PCP treatment group exhibited significantly enhanced SCX fluorescence signals in the injured area (Fig. 8A),

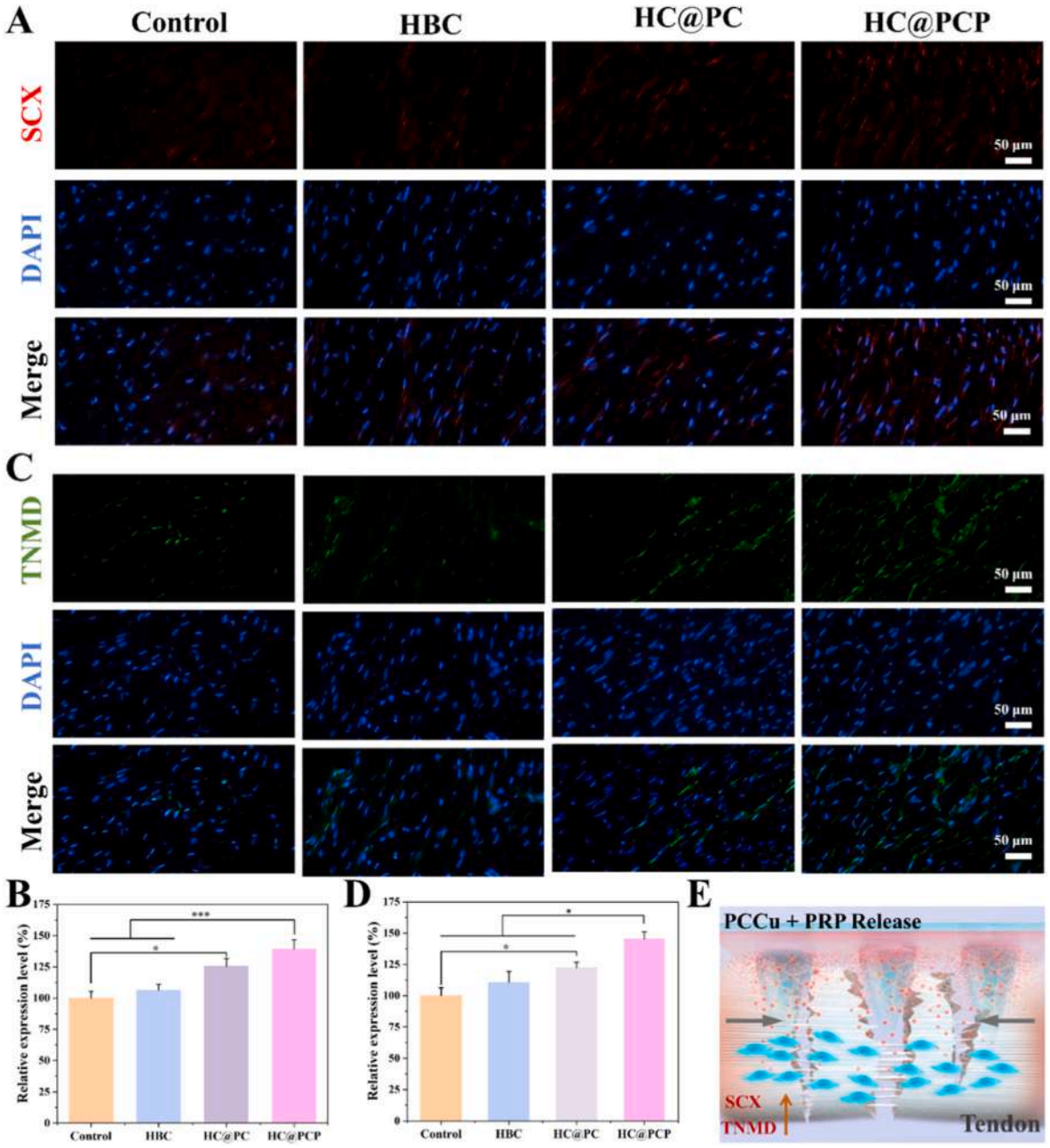

Fig. 8. HC@PCP regulates the expression of key tendon regeneration markers SCX and TNMD *in vivo*. (A) Representative immunofluorescence images of SCX in Achilles tendon tissues at 8 weeks post-operation. (B) Quantitative analysis of SCX immunofluorescence intensity at 8 weeks post-operation (n = 5). (C) Representative immunofluorescence images of TNMD in Achilles tendon tissues at 8 weeks post-operation. (D) Quantitative analysis of TNMD immunofluorescence intensity at 8 weeks post-operation (n = 5). (E) Schematic diagram illustrating the mechanism by which HC@PCP promotes tendon healing through synergistic upregulation of SCX and TNMD expression. $^{*}p < 0.05$, $^{**}p < 0.01$, $^{***}p < 0.001$.

indicating that HC@PCP activates endogenous tendon stem cells and promotes their directed differentiation toward the tendon lineage. Additionally, SCX expression in the HC@PC group was significantly elevated compared with the control group (Fig. 8B, $p < 0.01$). TNMD, a maturation marker protein involved in collagen fiber assembly and tendon mechanical architecture, exhibited markedly enhanced fluorescence signals in the injured region of the HC@PCP group compared to both the control and HBC groups (Fig. 8C and D, $p < 0.01$). This suggests that HC@PCP not only initiates the tendon differentiation program but also propels the newly formed tissue toward functional maturation. Collectively, these findings demonstrate that HC@PCP synergistically upregulates SCX and TNMD expression within the injured microenvironment, thereby systematically promoting tendon stem cell differentiation and the synthesis of functional tendon proteins (Fig. 8E).

Tendon samples were subjected to biomechanical testing to assess the effect of HC@PCP microneedles on postoperative tendon regeneration. As shown in Figs. S10 and S11, at 8 weeks post-operation, the HC@PCP group exhibited the highest maximum load and Young's modulus among all groups, which were significantly greater than those of the Control group ($p < 0.05$). Even the HC@PC group without PRP showed significantly higher maximum load and Young's modulus than the Control group ($p < 0.05$). In contrast, no significant difference was observed between the HBC microneedle group and the Control group. Moreover, the HC@PCP treatment group exhibited significantly higher failure strain than the control groups (Fig. S12). The improved failure strain indicates enhanced deformability and toughness of the repaired tendon tissue. These results are consistent with the observed increases in failure load and Young's modulus, collectively demonstrating that the sequential defense-nutrition strategy effectively enhances the overall mechanical integrity and functional performance of injured tendons. In summary, PCCu and PRP exerted a synergistic effect in promoting tendon healing, and the HC@PCP microneedles co-loaded with PCCu and PRP effectively promote tendon healing and restore favorable mechanical properties. In addition, to assess potential *in vivo* toxicity during long-term intervention with HC@PCP, major organ samples (heart, liver, spleen, lungs, and kidneys) were collected from rats at week 8 and systematically examined by hematoxylin and eosin (H&E) staining for histomorphological analysis. The results showed no significant pathological alterations or structural damage in any of the examined organs between the control group and the HC@PCP-treated group (Fig. S13), indicating that HC@PCP did not induce notable tissue toxicity under the experimental conditions and exhibited favorable *in vivo* biosafety.

The repair results from the rat Achilles tendon injury model in this study demonstrate the significant therapeutic advantages of the sequential defense-nutrition synergy strategy based on thermosensitive core-shell microneedles. In the early postoperative phase, the rapid release of PCCu from the microneedle shell effectively suppressed local inflammation. Histological analysis revealed that the HC@PCP group had a significantly lower inflammatory cell density compared with the control group, thereby creating a stable microenvironment for subsequent repair. Concurrently, the sustained release of PRP from the core provided long-term bioactive signaling support to tendon-derived stem cells, promoting tenogenic differentiation and extracellular matrix synthesis. This was evidenced by upregulation of key markers such as SCX and TNMD, along with progressively aligned collagen fibers in the injured tissue. At the 8-week endpoint, the HC@PCP group exhibited a denser and more regularly aligned collagen architecture. This was accompanied by significant upregulation of the key tenogenic markers SCX and TNMD *in vivo*, along with superior biomechanical properties. Collectively, these results demonstrate that the temporally controlled delivery strategy of PCCu and PRP not only accelerated the tissue repair process but also promoted the coordinated structural and functional maturation of the regenerated tendon. This “anti-inflammatory first, regeneration-promoting afterward” staged intervention matches the physiological timeline of tendon healing, thereby achieving synergistic enhancement of repair outcomes in deep tissue.

4. Discussion

Tendon repair after injury is a highly time-dependent biological process. Imbalanced oxidative stress and infection risk in the early stage can aggravate inflammatory tissue damage [51]. In the later stage, insufficient bioactive signals lead to disordered collagen arrangement and inadequate mechanical properties, which ultimately limit functional regeneration [52]. Currently, various biomaterial strategies (electrospun scaffolds, 3D-printed constructs, hydrogels, microspheres) have been developed for tendon repair, either alone or combined with cells/growth factors [53]. However, recent reviews highlight critical limitations: most scaffolds are only validated in animals with poor clinical translatability, non-degradable scaffolds offer robust mechanics but lack biocompatibility, while biodegradable ones fail to withstand tendon's dynamic stress [54]. Meanwhile, accelerating angiogenesis to ensure sufficient nutrient supply at the tendon injury site is also critical for expediting healing [55]. To address these issues, researchers emphasize two priorities: optimizing scaffolds for integrated mechanics, biocompatibility and safety and clarifying therapeutic mechanisms amid the multi-factorial nature of *in vivo* repair [54]. The sequential “defense-nutrition” strategy proposed by the thermosensitive core-shell microneedle system constructed in this study is designed to address this clinical need, and it is highly consistent with cutting-edge research concepts in the field. Compared with traditional single-function repair materials, this system achieves precise temporal regulation of the rapid early release of PCCu and the sustained late release of PRP through the synergistic effect of the core-shell structure and thermosensitive phase transition. This design concept has been widely supported by recent studies on intelligent delivery systems [56,57]. Existing research shows that the sequential release of antioxidants, antibacterial factors and growth factors can effectively simulate the physiological tendon repair process and significantly improve collagen deposition and mechanical reconstruction [58]. The *in vivo* experimental results of this study also confirm that this sequential strategy can effectively reduce inflammatory responses and promote ordered collagen arrangement, which is consistent with the above key research conclusions. Meanwhile, the precise anchoring of this system achieved through thermosensitive in situ gelation solves the problem of easy displacement of traditional microneedles and hydrogel carriers in dynamic deep soft tissues such as the Achilles tendon. It makes up for the deficiency of existing delivery systems in tissue adaptability and provides a new solution for spatiotemporally controlled repair of tendon regeneration.

Compared with conventional microneedle technologies based on chemical or photo-crosslinking strategies, this system exhibits remarkable distinctions and advantages in terms of application manner, drug release behavior, and biological safety [57,59]. The core innovation lies in the organic integration of material intelligence, structural engineering, and therapeutic rationale. In terms of application modality, traditional crosslinked microneedles (e.g., UV-cured systems) require prefabrication into fixed shapes *in vitro*. When implanted into deep, dynamic, and irregularly shaped soft tissues (such as the Achilles tendon), they frequently undergo displacement or exert mechanical stress on surrounding tissues due to mismatched mechanical properties, thereby impairing long-term retention and therapeutic efficacy. By exploiting the thermosensitive sol-gel transition of HBC (LCST $\approx 27\ ^{\circ}C$), the present system enables in situ physical gelation of microneedles at physiological temperature (37 °C) following tissue penetration, forming a three-dimensional network with mechanical properties matching those of the surrounding tissue. This transition proceeds without external energy input or chemical initiators, achieving biomechanical interlocking and seamless interfacial integration between the microneedle matrix and tissue. It effectively solves the problem of poor anchoring stability in dynamic soft tissues, a major limitation of traditional delivery systems. Regarding the regulation of drug release, drug delivery from conventional microneedles mostly relies on intrinsic material degradation, leading to simple and fixed release kinetics that

cannot well meet the biological needs of different stages during tissue repair. In this study, a sequential "defense-nutrition" release profile is established by combining core-shell structural design with the dynamic phase transition behavior of thermosensitive gels. After implantation, the metal-phenolic network (PCCu) loaded in the shell layer is rapidly released through diffusion channels formed during the initial gelation stage, promptly scavenging reactive oxygen species and inhibiting bacterial infection to rapidly establish an anti-inflammatory and anti-infective microenvironment. Subsequently, platelet-rich plasma (PRP) enriched with growth factors and encapsulated in the core is sustainably released after the gel network stabilizes, providing long-term biological signals for the proliferation and differentiation of tendon stem cells. This spatiotemporally controlled release creates a continuous process from microenvironment regulation to cell behavior guidance, which is highly consistent with the natural process of tendon regeneration. At the level of biocompatibility and translational potential, chemical or photo-crosslinked microneedles may contain residual crosslinkers, photoinitiators, or their degradation products. In addition, UV irradiation itself may cause cytotoxicity or local inflammation, raising long-term safety risks. In contrast, relying on the temperature-responsive physical gelation of HBC, this system involves no chemical crosslinking reagents or external irradiation. The HBC itself exhibits favorable biodegradability and biocompatibility, which significantly enhances the biosafety of the system and provides a crucial guarantee for its clinical translation. In addition, the loading dose of copper ions in PCCu was strictly controlled within a biosafe range in this study to avoid potential toxicity caused by excessive accumulation of free copper ions. Results of HE staining of major organs after surgery showed that no obvious pathological damage was observed in the heart, liver, spleen, lung, or kidney of the HC@PCP-treated group, with intact tissue structures. This directly confirms the safety of copper ions at this dose for *in vivo* application. From the perspective of metabolic mechanism, PCCu enables the mild and controllable release of copper ions. The released low-concentration copper ions can participate in the normal copper metabolism process of the body and be gradually eliminated through hepatic metabolism, biliary excretion, and renal excretion, without long-term accumulation *in vivo* [60,61]. Numerous studies on the application of copper-based biomaterials in tissue repair have confirmed that copper ions at an appropriate dose exert antioxidant, antibacterial, and pro-repair effects without obvious *in vivo* toxicity [30]. Consistent with the safety results of this study, these findings further support the clinical translation potential of the present system.

Notably, the therapeutic efficacy of the core-shell microneedle system (HC@PCP) was evaluated against a series of control groups, including the suture-only injury group, blank HBC microneedle group, and single-component HC@PC microneedle group. This allowed for the systematic dissection of the contributions from the carrier matrix, antioxidant/antibacterial components, and growth factor delivery. Due to experimental scope and model limitations, this study did not directly perform *in vivo* comparisons with clinically routine local platelet-rich plasma (PRP) injection. However, the rational design and performance of the present system offer distinct advantages over traditional high-dose injections. First, the thermosensitive in situ gelation property of HBC ensures stable anchoring at the tendon defect site, avoiding the common issue of rapid diffusion and clearance of bioactive factors in free PRP injections, which limits therapeutic efficacy. Second, the core-shell structure enables the sequential release of PCCu and PRP-derived growth factors, meeting the temporal requirements for early anti-inflammatory/anti-infective control and subsequent tendon regeneration. In contrast, a single PRP injection lacks such programmable delivery, often accompanied by burst release and short-term bioactivity [62,63]. Third, the co-delivery of defensive (PCCu) and regenerative (PRP) signals via a single implant achieves synergistic microenvironment regulation, which is difficult to accomplish in clinical practice by administering PRP and anti-inflammatory agents separately. These design advantages are supported by *in vitro* release data, as well as *in vivo* histological and biomechanical results, highlighting the potential of this core-shell microneedle system as a promising alternative or adjuvant to existing clinical strategies for tendon repair.

Compared with recently reported spatiotemporally controlled release systems such as bilayer scaffolds, microsphere-integrated hydrogels and gradient functional hydrogels, the core-shell microneedle system (HC@PCP) shows unique design advantages and application suitability [18,56,64,65]. Bilayer scaffolds are classic sequential drug delivery carriers. They mostly achieve stepwise release of bioactive substances by building layered structures through *in vitro* prefabrication [66]. However, their macroscopically rigid structure cannot perfectly fit deep, irregular and dynamic soft tissue injury sites like Achilles tendons. Implantation is relatively invasive. They also tend to shift under dynamic tissue mechanical forces, making stable local delivery difficult. Microsphere-integrated hydrogel systems disperse drug-loaded microspheres in a hydrogel matrix [67]. They can regulate multi-component release to a certain extent. But they have problems such as uneven spatial distribution of bioactive components, insufficient early rapid release efficiency and weak anchoring ability of hydrogels in deep tissues. These issues prevent them from fully meeting the temporal requirement for rapid defense in the early stage of injury. Gradient functional hydrogels mostly rely on chemical modification or component diffusion to build concentration gradients [68]. Their controlled release precision is limited. They also lack the ability for minimally invasive implantation and in situ adaptive shaping, which reduces convenience for clinical translation. In contrast, the HBC-based thermosensitive core-shell microneedle system constructed in this study integrates multiple technical advantages. First, the solid needle structure enables minimally invasive implantation without complex surgical operations. This is consistent with the development trend of clinical minimally invasive treatment. Second, relying on the body temperature-responsive sol-gel transition of HBC, the microneedles can undergo in situ adaptive gelation at the injury site after implantation. They form tight mechanical adaptation and stable anchoring with surrounding tissues. This completely solves the technical bottleneck of easy displacement and detachment of traditional delivery carriers in dynamic deep soft tissues. Third, the precise spatial compartmentalization of the core-shell structure works synergistically with the phase transition behavior of the thermosensitive hydrogel. This achieves programmed sequential delivery. PCCu in the shell layer is released rapidly in the early stage. PRP in the core layer is released continuously in the later stage. This precisely matches the physiological temporal requirement of "first defense, then nutrition" for tendon injury repair. Fourth, the purely physical thermosensitive gelation process does not require chemical crosslinkers or external energy input. It ensures excellent biocompatibility and safety for clinical translation. In summary, the sequential delivery strategy of this study exhibits significant advantages in minimally invasive delivery, in situ precise anchoring, sequential controlled release precision and adaptability to deep soft tissues.

5. Conclusion

This study developed an intelligent delivery system based on thermosensitive core-shell microneedles. By integrating the physical solidification property of thermosensitive HBC, the antioxidant and antibacterial functions of the metal-phenolic network (PCCu), and the pro-regenerative effects of multiple growth factors in PRP, an innovative "sequential defense-nutrition" synergistic repair strategy was proposed. The outer PCCu layer responds rapidly in the early stage of injury, effectively scavenging reactive oxygen species and inhibiting bacterial proliferation, thereby significantly reducing local inflammation. Meanwhile, the inner PRP core, under the controlled sustained-release of the HBC hydrogel, continuously releases growth factors, systematically promoting tenogenic differentiation of tendon-derived stem cells and the orderly synthesis of extracellular matrix. *In vitro* experiments demonstrated that the system possesses excellent antioxidant and broad-

spectrum antibacterial activities, and effectively guides tendon-derived stem cells toward functional tenocyte differentiation. Animal experiments further verified the therapeutic potential of this strategy: in a rat Achilles tendon injury model, the microneedle system significantly reduced inflammatory cell infiltration, promoted densification and alignment of collagen fibers, and concurrently upregulated the expression of key tendon regeneration markers such as SCX and TNMD. These results indicate that the time-sequential delivery strategy successfully aligns with the physiological stages of tendon healing, achieving a synergistic effect between anti-inflammatory microenvironment construction and sustained regenerative signaling in deep tissue. This work provides a novel therapeutic strategy with minimally invasive characteristics, temporal controllability, and bioactivity for the functional regeneration of poorly vascularized tissues such as tendons, demonstrating promising translational potential in sports medicine and tissue engineering.

CRediT authorship contribution statement

Meimei Fu: Conceptualization, Data curation, Investigation, Methodology, Writing – original draft, Writing – review & editing. **Jintao Li:** Conceptualization, Data curation, Investigation, Methodology, Writing – review & editing. **Yiwen Jiang:** Conceptualization, Data curation, Methodology, Writing – original draft. **Yan Shao:** Data curation, Formal analysis, Resources, Software. **Dianxuan Wu:** Data curation, Software, Validation, Writing – original draft. **Shaozi Zhong:** Data curation, Investigation, Methodology. **Zhuoyi Huang:** Formal analysis, Investigation, Validation, Writing – original draft. **Chao Chen:** Data curation, Methodology, Validation. **Jinshan Guo:** Funding acquisition, Resources, Supervision, Writing – review & editing. **Denghui Xie:** Conceptualization, Funding acquisition, Supervision, Writing – review & editing. **Chun Zeng:** Conceptualization, Funding acquisition, Project administration, Resources, Supervision, Writing – review & editing.

Declaration of competing interest

The authors declare that they have no known competing financial interests or personal relationships that could have appeared to influence the work reported in this paper.

Acknowledgements

This work was supported by the Natural Science Foundation of China (Grant No. 81974328), Natural Science Funds for Distinguished Young Scholar of Guangdong province (Grant No. 2022B1515020044), the Guangdong Basic and Applied Basic Research Foundation (Grant No. 2024A1515012664), the Natural Science Foundation of Guangdong Province (Grant No. 2024A1515011231) and the Clinical Research Special Fund of the president's Foundation of the Third Affiliated Hospital of Southern Medical University (Grant No. YL202206).

Appendix B. Supplementary data

Supplementary data to this article can be found online at https://doi.org/10.1016/j.mtbio.2026.102964.

Data availability

Data will be made available on request.

References

[1] C. Ouyang, T. Tu, H. Yu, L. Wang, Z. Ni, J. Yang, Y. Dong, X. Zou, W. Zhou, J. Liu, D. Chen, Y. Wang, X. Wu, H. Yi, X. Yuan, Z. Liu, H. Lu, One-step formed janus hydrogel with time-space regulating properties for suture-free and high-quality tendon healing, Adv. Sci. 12 (13) (2025) e2411400, https://doi.org/10.1002/advs.202411400.

[2] A. Bedi, J. Bishop, J. Keener, D.A. Lansdown, O. Levy, P. MacDonald, N. Maffulli, J. H. Oh, V.J. Sabesan, J. Sanchez-Sotelo, R.J. Williams, B.T. Feeley, Rotator cuff tears, Nat. Rev. Dis. Primers 10 (1) (2024) 8, https://doi.org/10.1038/s41572-024-00492-3.

[3] M.A. Fernandez-Yague, A. Trotier, S. Demir, S.A. Abbah, A. Larrañaga, A. Thirumaran, A. Stapleton, S.A.M. Tofail, M. Palma, M. Kilcoyne, A. Pandit, M. J. Biggs, A self-powered piezo-bioelectric device regulates tendon repair-associated signaling pathways through modulation of mechanosensitive ion channels, Adv. Mater. 34 (14) (2022) e2201543, https://doi.org/10.1002/adma.202201543.

[4] B. Faustini, T. Lettner, A. Wagner, H. Tempfer, N.P. Cesur, C. Lehner, C. Brouwer, K. Roelofs, O. Mykhailyk, C. Plank, J. Rip, R. Gehwolf, A. Traweger, Improved tendon repair with optimized chemically modified mRNAs: combined delivery of Pdgf-BB and IL-1Ra using injectable nanoparticles, Acta Biomater. 195 (2025) 451–466, https://doi.org/10.1016/j.actbio.2025.02.025.

[5] L. Chen, M. Cai, S. Lin, M. Li, Z. Zhu, H. Zhang, H. Zhao, C. Xu, R. Yang, Lymphatic-stem cell crosstalk promotes tendon regeneration via Notch1-Srebp2-mediated cholesterol metabolism, Nat. Commun. (2025), https://doi.org/10.1038/s41467-025-67898-9.

[6] G. Nourissat, F. Berenbaum, D. Duprez, Tendon injury: from biology to tendon repair, Nat. Rev. Rheumatol. 11 (4) (2015) 223–233, https://doi.org/10.1038/nrrheum.2015.26.

[7] Q. Su, H. Ge, J. Li, C. Liu, L. Chen, J. Li, Q. Cai, C. Huang, X. Feng, D. Li, B. Cheng, Temporal vascular pattern remodeling mediated by the FHL2/sFRP2 signaling pathway in tenocytes affects tendon repair and regeneration, Exp. Mol. Med. 57 (11) (2025) 2533–2558, https://doi.org/10.1038/s12276-025-01574-2.

[8] E. Gracey, A. Burssens, I. Cambré, G. Schett, R. Lories, I.B. McInnes, H. Asahara, D. Elewaut, Tendon and ligament mechanical loading in the pathogenesis of inflammatory arthritis, Nat. Rev. Rheumatol. 16 (4) (2020) 193–207, https://doi.org/10.1038/s41584-019-0364-x.

[9] X. Gao, S. Wu, Z. Yao, Y. Shao, J. Feng, Z. Yuan, H. Mao, Engineered decellularized tendon hydrogel with sustained zinc ion release orchestrates anti-inflammatory microenvironment and functional regeneration in Achilles tendinopathy, Mater. Today Bio 34 (2025) 102104, https://doi.org/10.1016/j.mtbio.2025.102104.

[10] B. Chen, Y. Zhao, S. Guo, C. Tang, B. Xu, M. Zhou, Q. Chen, L. Ma, J. Lyu, L. Guo, Y. Wang, Tendon tissue engineering: pathophysiological mechanism and bioengineering therapy of tendinopathy, Int. J. Nanomed. 20 (2025) 12529–12571, https://doi.org/10.2147/ijn.S550439.

[11] G.P. Hess, W.L. Cappiello, R.M. Poole, S.C. Hunter, Prevention and treatment of overuse tendon injuries, Sports Med. 8 (6) (1989) 371–384, https://doi.org/10.2165/00007256-198908060-00005.

[12] J. Chen, R. Sheng, Q. Mo, L.J. Backman, Z. Lu, Q. Long, Z. Chen, Z. Cao, Y. Zhang, C. Liu, H. Zheng, Y. Qi, M. Cao, Y. Rui, W. Zhang, Controlled TPCA-1 delivery engineers a pro-tenogenic niche to initiate tendon regeneration by targeting IKKβ/NF-κB signaling, Bioact. Mater. 44 (2024) 319–338, https://doi.org/10.1016/j.bioactmat.2024.10.016.

[13] B. Chalidis, P. Givissis, P. Papadopoulos, C. Pitsilos, Molecular and biologic effects of platelet-rich plasma (PRP) in ligament and tendon healing and regeneration: a systematic review, Int. J. Mol. Sci. 24 (3) (2023), https://doi.org/10.3390/ijms24032744.

[14] C.H. Chen, S.H. Chen, S.H. Chen, A.D. Chuang, G.D. T, J.P. Chen, Hyaluronic acid/platelet rich plasma-infused core-shell nanofiber membrane to prevent postoperative tendon adhesion and promote tendon healing, Int. J. Biol. Macromol. 231 (2023) 123312, https://doi.org/10.1016/j.ijbiomac.2023.123312.

[15] P.A. Everts, J.F. Lana, R.W. Alexander, I. Dallo, E. Kon, M.A. Ambach, A. van Zundert, L. Podesta, Profound properties of protein-rich, platelet-rich plasma matrices as novel, multi-purpose biological platforms in tissue repair, regeneration, and wound healing, Int. J. Mol. Sci. 25 (14) (2024), https://doi.org/10.3390/ijms25147914.

[16] J. Li, H. Ke, X. Lei, J. Zhang, Z. Wen, Z. Xiao, H. Chen, J. Yao, X. Wang, Z. Wei, H. Zhang, W. Pan, Y. Shao, Y. Zhao, D. Xie, C. Zeng, Controlled-release hydrogel loaded with magnesium-based nanoflowers synergize immunomodulation and cartilage regeneration in tendon-bone healing, Bioact. Mater. 36 (2024) 62–82, https://doi.org/10.1016/j.bioactmat.2024.02.024.

[17] R. Zhang, H. Li, Y. Mu, R. Li, X. Li, T. Gao, Y. Yang, Z. Xu, Y. Ren, C. Ning, Z. Zhao, L. Hao, Q. Guo, S. Liu, Turmeric-derived extracellular vesicles loaded microneedle system attenuates rotator cuff degeneration by orchestrating energetic metabolism, Mater. Today Bio 35 (2025) 102590, https://doi.org/10.1016/j.mtbio.2025.102590.

[18] Q. Zhang, Y. Yang, D. Suo, S. Zhao, J.C. Cheung, P.H. Leung, X. Zhao, A biomimetic adhesive and robust janus patch with anti-oxidative, anti-inflammatory, and anti-bacterial activities for tendon repair, ACS Nano 17 (17) (2023) 16798–16816, https://doi.org/10.1021/acsnano.3c03556.

[19] Y.A. Mao, S. Xu, X. Shi, Y. Jin, Z. Pan, T. Hao, G. Li, X. Chen, H. Wang, Y. Wang, J. Xiao, Bioengineered microneedles and nanomedicine as therapeutic platform for tissue regeneration, J. Nanobiotechnol. 23 (1) (2025) 573, https://doi.org/10.1186/s12951-025-03623-4.

[20] A.P. Singh, A. Biswas, A. Shukla, P. Maiti, Targeted therapy in chronic diseases using nanomaterial-based drug delivery vehicles, Signal Transduct. Targeted Ther. 4 (2019) 33, https://doi.org/10.1038/s41392-019-0068-3.

[21] Z. Li, K. Xu, L. Qin, D. Zhao, N. Yang, D. Wang, Y. Yang, Hollow nanomaterials in advanced drug delivery systems: from Single- to multiple shells, Adv. Mater. 35 (12) (2023) e2203890, https://doi.org/10.1002/adma.202203890.

[22] M. Rasekh, M.S. Arshad, Z. Ahmad, Advances in drug delivery integrated with regenerative medicine: innovations, challenges, and future frontiers, Pharmaceutics 17 (4) (2025), https://doi.org/10.3390/pharmaceutics17040456.

[23] T. Lv, Y. Chen, N. Li, X. Liao, Y. Heng, Y. Guo, K. Hu, A comprehensive review of thermosensitive hydrogels: mechanism, optimization strategies, and applications, Gels 11 (7) (2025), https://doi.org/10.3390/gels11070544.
[24] J. Shan, Y. Yu, X. Liu, Y. Chai, X. Wang, G. Wen, Recent advances of chitosan-based composite hydrogel materials in application of bone tissue engineering, Heliyon 10 (19) (2024) e37431, https://doi.org/10.1016/j.heliyon.2024.e37431.
[25] J. Chen, X. Guan, L. Chen, B. Zheng, F. Li, C. Fang, Y. Fu, X. Li, H. Wang, Y. Zhou, Customized hydrogel system for the spatiotemporal sequential treatment of periodontitis propelled by ZEB1, Adv. Sci. 12 (26) (2025) e2503338, https://doi.org/10.1002/advs.202503338.
[26] M. Lei, H. Liu, Q. Zhong, L. Zhao, J. Liu, H. Mai, Y. Zhang, H. Wang, Y. Chen, R. Chen, Y. Xu, H. Li, D. Wang, J. Gao, S. Zheng, Z. Shi, J. Wang, H. Cheng, Hydroxybutyl chitosan-based thermosensitive hydrogel enhanced osteoporotic bone regeneration through sustained release of alendronate and BMP-2, Carbohydr. Polym. 373 (2026) 124609, https://doi.org/10.1016/j.carbpol.2025.124609.
[27] Y. Sun, L. Yang, L. Du, Y. Zhou, K. Xu, J. Chen, Y. He, Q. Qu, Y. Miao, M. Xing, Z. Hu, Duo-role Platelet-rich plasma: temperature-induced fibrin gel and growth factors' reservoir for microneedles to promote hair regrowth, J. Adv. Res. 55 (2024) 89–102, https://doi.org/10.1016/j.jare.2023.02.014.
[28] J.Y. Li, Y.H. Feng, Y.T. He, L.F. Hu, L. Liang, Z.Q. Zhao, B.Z. Chen, X.D. Guo, Thermosensitive hydrogel microneedles for controlled transdermal drug delivery, Acta Biomater. 153 (2022) 308–319, https://doi.org/10.1016/j.actbio.2022.08.061.
[29] M. Fu, Y. Zhao, Y. Wang, Y. Li, M. Wu, Q. Liu, Z. Hou, Z. Lu, K. Wu, J. Guo, On-Demand removable self-healing and pH-Responsive europium-releasing adhesive dressing enables inflammatory microenvironment modulation and angiogenesis for diabetic wound healing, Small 19 (3) (2023) e2205489, https://doi.org/10.1002/smll.202205489.
[30] M. Fu, Q. Xiang, Z. Huang, W. Luo, Z. Fang, J. Li, Y. Li, Z. Xia, Y. Huang, Y. Zhao, W. Liao, J. Guo, Photo-cross-linked and photothermal Flammulina velutipes polysaccharide hydrogel loaded with caffeic acid-copper nanozyme for diabetic wound healing, ACS Appl. Mater. Interfaces 17 (38) (2025) 53145–53167, https://doi.org/10.1021/acsami.5c11453.
[31] H. Wang, F. Song, J. Feng, X. Qi, L. Ma, L. Xie, W. Shi, Q. Zhou, Tannin coordinated nanozyme composite-based hybrid hydrogel eye drops for prophylactic treatment of multidrug-resistant Pseudomonas aeruginosa keratitis, J. Nanobiotechnol. 20 (1) (2022) 445, https://doi.org/10.1186/s12951-022-01653-w.
[32] Y. Wang, S. Jin, D. Luo, D. He, C. Shi, L. Zhu, B. Guan, Z. Li, T. Zhang, Y. Zhou, C. Y. Wang, Y. Liu, Functional regeneration and repair of tendons using biomimetic scaffolds loaded with recombinant periostin, Nat. Commun. 12 (1) (2021) 1293, https://doi.org/10.1038/s41467-021-21545-1.
[33] M. Sun, T. Wang, J. Pang, X. Chen, Y. Liu, Hydroxybutyl chitosan centered biocomposites for potential curative applications: a critical review, Biomacromolecules 21 (4) (2020) 1351–1367, https://doi.org/10.1021/acs.biomac.0c00071.
[34] Q.Q. Wang, M. Kong, Y. An, Y. Liu, J.J. Li, X. Zhou, C. Feng, J. Li, S.Y. Jiang, X. J. Cheng, X.G. Chen, Hydroxybutyl chitosan thermo-sensitive hydrogel: a potential drug delivery system, J. Mater. Sci. 48 (16) (2013) 5614–5623, https://doi.org/10.1007/s10853-013-7356-z.
[35] S. Bi, M. Kong, X. Cheng, X. Chen, Temperature sensitive self-assembling hydroxybutyl chitosan nanoparticles with cationic enhancement effect for multi-functional applications, Carbohydr. Polym. 254 (2021) 117199, https://doi.org/10.1016/j.carbpol.2020.117199.
[36] C. Chen, W. Zhang, Y. Zhang, P. Wang, F. Ren, Tunable thermo-responsive properties of hydroxybutyl chitosan oligosaccharide, Front. Chem. 10 (2022) 830516, https://doi.org/10.3389/fchem.2022.830516.
[37] S. Liu, R. Ju, Z. Zhang, Z. Jiang, J. Cui, W. Liu, B. Han, S. Wang, Temperature-sensitive injectable chitosan-based hydrogel for endoscopic submucosal dissection, Int. J. Biol. Macromol. 282 (2024) 136566, https://doi.org/10.1016/j.ijbiomac.2024.136566.
[38] M.C. Mañas-Torres, C. Gila-Vilchez, F.J. Vazquez-Perez, P. Kuzhir, D. Momier, J. C. Scimeca, A. Borderie, M. Goracci, F. Burel-Vandenbos, C. Blanco-Elices, I. A. Rodriguez, M. Alaminos, L. de Cienfuegos, M.T. Lopez-Lopez, Injectable magnetic-responsive short-peptide supramolecular hydrogels: ex vivo and in vivo evaluation, ACS Appl. Mater. Interfaces 13 (42) (2021) 49692–49704, https://doi.org/10.1021/acsami.1c13972.
[39] J. Li, Z. Deng, X. Liang, S. Zhong, H. Ke, Z. Wen, D. Wu, Y. Jiang, Z. Huang, Y. Shao, M. Fu, C. Zeng, A smart ROS-responsive hydrogel for on-demand antibacterial and platelet-rich plasma (PRP) activation in diabetic wound healing, J. Contr. Release 388 (Pt 2) (2025) 114392, https://doi.org/10.1016/j.jconrel.2025.114392.
[40] Q. Wu, D. Liu, X. Zhang, D. Wang, M. DongYe, W. Chen, D. Lin, F. Zhu, W. Chen, H. Lin, Development and effects of tacrolimus-loaded nanoparticles on the inhibition of corneal allograft rejection, Drug Deliv. 26 (1) (2019) 290–299, https://doi.org/10.1080/10717544.2019.1582728.
[41] A. Liu, Q. Wang, Z. Zhao, R. Wu, M. Wang, J. Li, K. Sun, Z. Sun, Z. Lv, J. Xu, H. Jiang, M. Wan, D. Shi, C. Mao, Nitric oxide nanomotor driving exosomes-loaded microneedles for achilles tendinopathy healing, ACS Nano 15 (8) (2021) 13339–13350, https://doi.org/10.1021/acsnano.1c03177.
[42] N.L. Millar, G.A. Murrell, I.B. McInnes, Inflammatory mechanisms in tendinopathy - towards translation, Nat. Rev. Rheumatol. 13 (2) (2017) 110–122, https://doi.org/10.1038/nrrheum.2016.213.
[43] S. Wang, Y. Liu, Q. Sun, B. Zeng, C. Liu, L. Gong, H. Wu, L. Chen, M. Jin, J. Guo, Z. Gao, W. Huang, Triple cross-linked dynamic responsive hydrogel loaded with selenium nanoparticles for modulating the inflammatory microenvironment via PI3K/Akt/NF-κB and MAPK signaling pathways, Adv. Sci. 10 (31) (2023) e2303167, https://doi.org/10.1002/advs.202303167.
[44] Y. Li, Y. Miao, L. Yang, G. Wang, M. Fu, Y. Wang, D. Fu, J. Huang, J. Wang, Z. Fan, Z. Lu, J. Guo, Z. Hu, Malate-based polyester chemically shielded metal-phenolic networks coated artificial hair fibers with long-lasting antimicrobial and anti-inflammatory performance, Chem. Eng. J. 455 (2023) 140572, https://doi.org/10.1016/j.cej.2022.140572.
[45] M.P. Tian, A.D. Zhang, Y.X. Yao, X.G. Chen, Y. Liu, Mussel-inspired adhesive and polypeptide-based antibacterial thermo-sensitive hydroxybutyl chitosan hydrogel as BMSCs 3D culture matrix for wound healing, Carbohydr. Polym. 261 (2021) 117878, https://doi.org/10.1016/j.carbpol.2021.117878.
[46] Y. Wang, Y. Zhao, S. Ma, M. Fu, M. Wu, J. Li, K. Wu, X. Zhuang, Z. Lu, J. Guo, Injective programmable proanthocyanidin-coordinated zinc-based composite hydrogel for infected bone repair, Adv. Healthcare Mater. 13 (6) (2024) e2302690, https://doi.org/10.1002/adhm.202302690.
[47] C. Mao, Y. Qiu, H. Sang, H. Mei, A. Zhu, J. Shen, S. Lin, Various approaches to modify biomaterial surfaces for improving hemocompatibility, Adv. Colloid Interface Sci. 110 (1-2) (2004) 5–17, https://doi.org/10.1016/j.cis.2004.02.001.
[48] Y. He, J. Sheng, F. Liu, F. Li, S. Lu, W. Chen, L. Yang, P. Zhou, Z. Chen, S. Chen, Z. Luo, J. Sun, SHED-derived exosome-mimetics promotes rotator cuff tendon-bone healing via macrophage immunomodulation through NF-κB suppression and autophagy activation, Mater. Today Bio 34 (2025) 102146, https://doi.org/10.1016/j.mtbio.2025.102146.
[49] M. Lin, W. Li, X. Ni, Y. Sui, H. Li, X. Chen, Y. Lu, M. Jiang, C. Wang, Growth factors in the treatment of Achilles tendon injury, Front. Bioeng. Biotechnol. 11 (2023) 1250533, https://doi.org/10.3389/fbioe.2023.1250533.
[50] R. Yang, G. Li, C. Zhuang, P. Yu, T. Ye, Y. Zhang, P. Shang, J. Huang, M. Cai, L. Wang, W. Cui, L. Deng, Gradient bimetallic ion-based hydrogels for tissue microstructure reconstruction of tendon-to-bone insertion, Sci. Adv. 7 (26) (2021), https://doi.org/10.1126/sciadv.abg3816.
[51] F. Jiang, H. Zhao, P. Zhang, Y. Bi, H. Zhang, S. Sun, Y. Yao, X. Zhu, F. Yang, Y. Liu, S. Xu, T. Yu, X. Xiao, Challenges in tendon-bone healing: emphasizing inflammatory modulation mechanisms and treatment, Front. Endocrinol. 15 (2024) 1485876, https://doi.org/10.3389/fendo.2024.1485876.
[52] Y. Jiang, C. Zhu, X. Ma, D. Fan, Tough and anisotropic janus hydrogel for tendon injury repair with controlled release of bFGF in tendon microenvironment, Chem. Eng. J. 500 (2024) 157139, https://doi.org/10.1016/j.cej.2024.157139.
[53] X. Jiang, S. Wu, M. Kuss, Y. Kong, W. Shi, P.N. Streubel, T. Li, B. Duan, 3D printing of multilayered scaffolds for rotator cuff tendon regeneration, Bioact. Mater. 5 (3) (2020) 636–643, https://doi.org/10.1016/j.bioactmat.2020.04.017.
[54] X. Yu, J. Cui, Y. Shen, W. Guo, P. Cai, Y. Chen, Z. Yuan, M. Liu, M. El-Newehy, H. El-Hamshary, Y. Morsi, B. Sun, M. Shafiq, X. Mo, Current advancements and strategies of biomaterials for tendon repair: a review, Front. Biosci. 28 (4) (2023) 66, https://doi.org/10.31083/j.fbl2804066.
[55] X. Liu, B. Zhu, Y. Li, X. Liu, S. Guo, C. Wang, S. Li, D. Wang, The role of vascular endothelial growth factor in tendon healing, Front. Physiol. 12 (2021) 766080, https://doi.org/10.3389/fphys.2021.766080.
[56] M. Fu, Y. Li, Y. Zhao, Y. Zhu, Z. Fang, Z. Huang, W. Luo, X. Huang, J. Li, Z. Hu, K. Wu, J. Guo, Janus adhesive dressing with macro/micro dual design enabling sequential microenvironment regulation for scarless wound healing, Adv. Fiber Mater. 8 (1) (2026) 262–288, https://doi.org/10.1007/s42765-025-00620-y.
[57] Y. Zhang, S. Wang, Y. Yang, S. Zhao, J. You, J. Wang, J. Cai, H. Wang, J. Wang, W. Zhang, J. Yu, C. Han, Y. Zhang, Z. Gu, Scarless wound healing programmed by core-shell microneedles, Nat. Commun. 14 (1) (2023) 3431, https://doi.org/10.1038/s41467-023-39129-6.
[58] L.L. Zhao, J.J. Luo, J. Cui, X. Li, R.N. Hu, X.Y. Xie, Y.J. Zhang, W. Ding, L.J. Ning, J. C. Luo, T.W. Qin, Tannic acid-modified decellularized tendon scaffold with antioxidant and anti-inflammatory activities for tendon regeneration, ACS Appl. Mater. Interfaces 16 (13) (2024) 15879–15892, https://doi.org/10.1021/acsami.3c19019.
[59] M. Teng, L. Zhang, Y. Fan, M. Fu, Z. Li, Microneedles loaded with PD-L1 inhibitor and doxorubicin GelMA hydrogel for melanoma immunochemotherapy, Mater. Des. 255 (2025) 114238, https://doi.org/10.1016/j.matdes.2025.114238.
[60] K. Yin, B. Li, X. Wang, W. Zhang, L. Chen, Ultrasensitive colorimetric detection of Cu2+ ion based on catalytic oxidation of L-cysteine, Biosens. Bioelectron. 64 (2015) 81–87, https://doi.org/10.1016/j.bios.2014.08.058.
[61] C. Wijmenga, L.W. Klomp, Molecular regulation of copper excretion in the liver, Proc. Nutr. Soc. 63 (1) (2004) 31–39, https://doi.org/10.1079/pns2003316.
[62] H.T. Lu, W.T. Chang, M.L. Tsai, C.H. Chen, W.Y. Chen, F.L. Mi, Development of injectable fucoidan and biological macromolecules hybrid hydrogels for intra-articular delivery of platelet-rich plasma, Mar. Drugs 17 (4) (2019), https://doi.org/10.3390/md17040236.
[63] S. Zare, A. Jafarzadeh, S. Zare, A. Shamloo, Exploring the dermatological applications of human mesenchymal stem cell secretome: a comprehensive review, Stem Cell Res. Ther. 16 (1) (2025) 177, https://doi.org/10.1186/s13287-025-04311-8.
[64] J. Zhang, Y. Zheng, J. Lee, J. Hua, S. Li, A. Panchamukhi, J. Yue, X. Gou, Z. Xia, L. Zhu, X. Wu, A pulsatile release platform based on photo-induced imine-crosslinking hydrogel promotes scarless wound healing, Nat. Commun. 12 (1) (2021) 1670, https://doi.org/10.1038/s41467-021-21964-0.
[65] X. Huang, J. Liang, Q. Jia, K. Qin, J. Shi, Z. Fan, A 3D-Printed piezoelectric scaffold with bio-inspired gradient and dynamic adaptation for tendon regeneration, Adv. Mater. (2026) e17298, https://doi.org/10.1002/adma.202517298.

[66] L. Wang, Y. Liu, Z. Lin, H. Chen, B. Liu, X. Yan, T. Zhu, Q. Zhang, J. Zhao, Durable immunomodulatory hierarchical patch for rotator cuff repairing, Bioact. Mater. 37 (2024) 477–492, https://doi.org/10.1016/j.bioactmat.2024.03.029.

[67] M. Yang, C. Zhang, B.Y. Lu, Y.C. Zhu, X.R. Fu, Y. Wu, Z.T. Zheng, C.S. Liu, J. Cheng, H.J. Huang, J.Q. Wang, Injectable composite microspheres/hydrogel membranes for achilles tendon regeneration, Mater. Today Bio 34 (2025) 102129, https://doi.org/10.1016/j.mtbio.2025.102129.

[68] X. Wang, S. Wu, R. Li, H. Yang, Y. Sun, Z. Cao, X. Chen, Y. Hu, H. Zhang, Z. Geng, L. Bai, Z. Shi, K. Xu, H. Tan, J. Su, ROS-activated nanohydrogel scaffolds with multi-factors controlled release for targeted dual-lineage repair of osteochondral defects, Adv. Sci. 12 (20) (2025) e2412410, https://doi.org/10.1002/advs.202412410.